



Structured light patterns in active stereo vision system
for the PIRATE robot

M.P. (Thijs) Bastiaens

BSc Report

Committee:

Dr.ir. J.B.C. Engelen
N. Botteghi, MSc
Dr.ir. P.C. Breeveld
Dr. H.K. Hemmes

September 2018

037RAM2018
Robotics and Mechatronics
EE-Math-CS
University of Twente
P.O. Box 217
7500 AE Enschede
The Netherlands

Structured light patterns in active stereo vision system for the PIRATE robot

Thijs Bastiaens
Robotics and Mechatronics
Advanced Technology, University Of Twente

September 4, 2018

Abstract

The aim of the Pipe Inspection Robot for Autonomous Exploration (PIRATE) project is to develop an autonomous robot platform for in-pipe inspection of small diameter, low pressure (urban) gas distribution mains. In order to assess the quality of the pipe detailed information on condition of the network and accurate location of deformation of the pipes, bends and dents is needed. Furthermore, the distances, number of branches and radii of intersections is needed for the robot to autonomously travel the network. This thesis describes the development of an Active Stereo Vision measurement setup which is used to test the effectiveness of different light patterns in different pipe setups. The presented patterns are all composed of circles, allowing for the setup to be recreated using lasers instead of a projector. Image processing algorithms are used to extract features from the measurement image and to reconstruct the pipe's inner surface.

Contents

1	Introduction	2
1.1	Smart Tooling	2
1.2	Problem Context	2
1.3	PIRATE	2
1.4	Previous work	3
1.5	Research question	3
1.6	Report outline	3
2	Background	4
2.1	Pinhole camera model	4
2.1.1	Geometry	4
2.1.2	Camera matrix	6
2.1.3	Distortion	6
2.1.4	Field of view	7
2.2	Active Stereo Vision	7
2.2.1	Coordinate transformation	7
2.2.2	Optical Triangulation	8
2.2.3	Epipolar Geometry	9
2.3	Configurations	10
2.3.1	Configuration I	10
2.3.2	Configuration II	12
2.4	Measurement Range	13
3	Analysis	14
3.1	Error analysis	14
3.1.1	Sampling error	14
3.1.2	Calibration error	15
3.2	System calibration	15
3.2.1	Camera matrix	15
3.2.2	Extrinsic ASV parameters	16
3.2.3	Projector Matrix and t_z	17
3.3	Patterns	18
3.3.1	Generating patterns	18
3.3.2	Parameters of patterns	19
3.3.3	Colors of patterns	20
3.4	Image processing	20
3.4.1	Undistortion	21
3.4.2	Median filter	21
3.4.3	Threshold	22
3.4.4	Object selection	22
3.4.5	Dilation	24
3.4.6	Intensity adjustment	24

3.4.7	Polar transform	24
3.4.8	Intensity weighted fit	25
3.4.9	Reconstruction	26
4	Design	27
4.1	Equipment	27
4.2	Measurement structure	27
4.3	Pipe setups	27
4.4	Experiment design	28
5	Results	30
5.1	Straight, Bend and T-section I	30
5.2	Curve	30
5.3	T-section II	31
5.4	Errors	31
6	Final considerations	32
6.1	Discussion	32
6.2	Conclusion	35
6.3	Recommendations	35
7	Appendix	37
7.1	Table of symbols & units	37
7.2	ASV structure design	37
7.3	Code	40
7.4	Results	43

1 Introduction

1.1 Smart Tooling

'Smart Tooling' is a project in the European program Interreg Vlanders-Netherlands. The project aims to improve automation in the process industry by making maintenance safer, cheaper, cleaner and more efficient. This is accomplished by providing funding to small companies to stimulate innovation and development in the robot technology field. The R&D topics these companies invest in are inspection robots, cleaning robots, shared workspace robots, and unmanned aerial systems .

The Knowledge and Innovation Center for Maintenance in the Process industry coordinates the Smart Tooling project and collaborates with partners from the industry and academia. One of these academic partners is the University of Twente, specifically the Robotics and Mechatronics (RaM) research group.[1][2]

1.2 Problem Context

The network of gas distribution pipes in the Netherlands is checked for leaks every 5 years. Passive data loggers or pipe inspection gauges are often used in the high-pressure distribution mains. This method does not apply to the low-pressure network, because these pipes have a smaller diameter and a larger amount of bends, T-joints and other types of intersections. Therefore, the low-pressure network, which spans over 100.000 km, is currently only inspected using above ground methods.

Since people don't fit inside the pipe, it is inspected from the outside, which can involve removing layers of isolation material. On top of that, the low-pressure network mostly occupies urban area, in which the risk for public health and safety are largest and replacements costs are highest. For this reason, it is important to have accurate data of the state of the pipes and precise information on the location and severity of leaks and damaged sections.[3]

1.3 PIRATE

Within the context of Smart Tooling, RaM works on the autonomous inspection of industrial pipelines in a project titled 'PIRATE', which stands for Pipe Inspection Robot for AuTonomous Exploration. This robot could be placed inside the pipe to carry out inspection, such that people are only needed to check and repair points of interests that were indicated by the robot. For this to happen, the robot needs to be energy efficient, be able to gather information on the location of defects and deformations, be able to measure the wall thickness and have the ability to navigate the network autonomously.[4] A previous iteration of the PIRATE robot can be seen in figure 1.

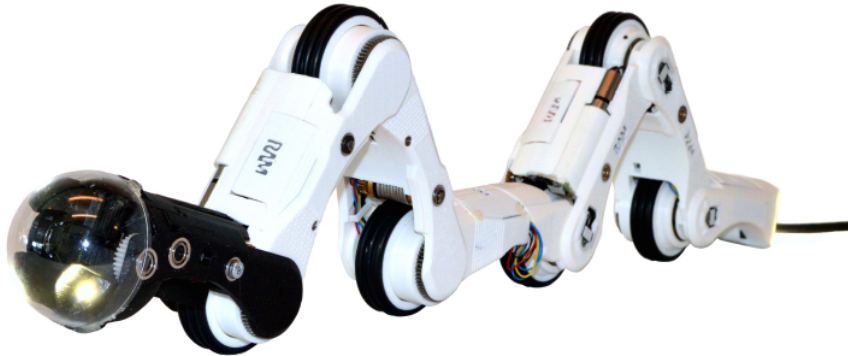


Figure 1: A previous design of PIRATE [7]

1.4 Previous work

The PIRATE project started in 2006 and so far a large number of people, companies and organizations have contributed.[4] Especially the work of Drost (2009)[5] and Reiling (2014)[6] is of interest, as it features the development of the vision system of PIRATE. In the current system, a monocular circular pattern of light, originating from a laser module, is reflected by a mirror and shone into the pipe. The reflection is recorded by a camera and subjected to image processing algorithms that extract the inner geometry of the pipe. Before use, the laser module, camera and mirror have to be aligned using a 3D printed mechanism.

1.5 Research question

The goal of this thesis is to find the optimal structured light pattern to use in a Active Stereo Vision (ASV), 2.2, system for the PIRATE robot. The pattern will be optimal in terms of robustness against errors in calibration of the intrinsic parameters, misalignment and quantization and its ability to detect obstacles, turns, bends and intersections.

1.6 Report outline

This report starts with modeling the ASV system as two pinhole camera's that are related via a coordinate transformation. It then proceeds by analyzing different configurations and their effects on the uncertainties in the ASV system. Next, procedures for calibration and image processing are given, together with a selection of patterns. After that the measurement setup is given, followed by a chapter summarizing the measurement procedure and results. The report closes with a discussion, a conclusion and recommendations for future work.

2 Background

The literature study begins with the pinhole camera model, which will be used to model the camera and projector that are used in the AVS system. In the next section, the basic principles for ASV will be presented. Then the various configurations, based on epipolar geometry, will be analyzed. Eventually the measurement range of an ASV system is derived.

2.1 Pinhole camera model

The pinhole camera model describes the relationship between the coordinates of a point in three-dimensional space and its location on an two-dimensional image plane. This relationship is only accurate for a pinhole camera, in which the camera aperture is a point and no lenses are used. The model does not include, for example, distortions and blurring of unfocused objects that are a result of lenses and finite-sized apertures. Furthermore, it does not account for quantization as a result of the cameras discrete image coordinates, called pixels. Therefore, the validity of the model depends on the quality of the camera and often decreases from the center of the image outwards[8].

A projector can be imagined as a 'reverse' camera. While the pinhole camera model is usually used to describe the mapping of a 3D scene point to a 2D image, it's inverse can be used to model a projector.

2.1.1 Geometry

Imagine an orthogonal coordinate system $\Psi \in \mathbb{R}^3$ with origin \mathbf{O} and axis $[X,Y,Z]$. The Z axis coincides with the viewing direction of the camera or projector and is called the optical axis.

An image plane ψ , parallel to the X and Y axis, with axis $[x,y]$, is located a distance F from the origin with respect to the optical axis, where F is the focal length of camera or projector. $\mathbf{R} = [x_r, y_r]$ is the point on the image plane where the optical axis and image plane intersect and is referred to as the principal point. Since this image plane represents a digital image, the origin of the plane will be chosen to be the top left corner and the units of the coordinates are pixels.

A point $\mathbf{P} = [X_p, Y_p, Z_p]$ exist somewhere in the world relative to $[X,Y,Z]$. The line from \mathbf{P} through \mathbf{O} intersects the image plane at point $\mathbf{Q} = [x_q, y_q]$ and is called the projection line. This geometry is illustrated in figure 2.

The point's coordinates are related to the image plane coordinates via[5]:

$$x_q = f_x \frac{X_p}{Z_p} + s \frac{Y_p}{Z_p} + x_r \quad (1)$$

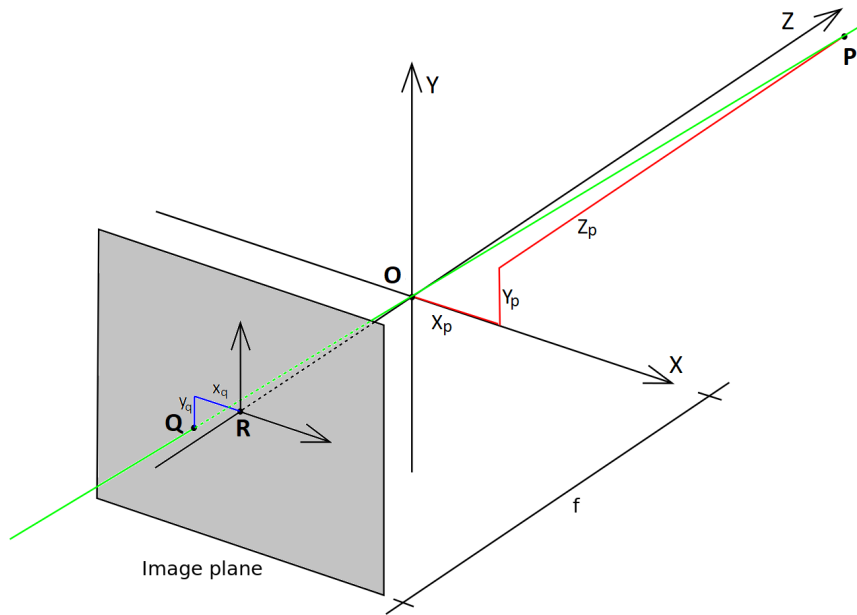


Figure 2: Geometry of the pinhole camera model[13]

$$y_q = f_y \frac{Y_p}{Z_p} + y_r \quad (2)$$

In this equation the skewness factor, s , is a measure of orthogonality of the camera plane coordinate frame. It is illustrated in figure 3 and can be expressed in number of pixels via[5]:

$$s = f_y \tan(\Phi) \quad (3)$$

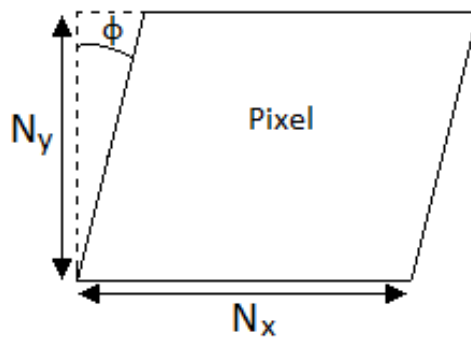


Figure 3: Skewness factor[14]

Furthermore, f_x and f_y are the normalized focal lengths, also in pixels. These are obtained by dividing the focal length F in of the objective lens by

the pixel dimensions in mm, n_x and n_y respectively:

$$\begin{pmatrix} f_x \\ f_y \end{pmatrix} = F \begin{pmatrix} \frac{1}{n_x} \\ \frac{1}{n_y} \end{pmatrix} \quad (4)$$

It should be noted that often times it can be assumed that the pixels are not skewed and square: $s = 0$, $n_x = n_y$, $f_x = f_y$. [6]

2.1.2 Camera matrix

The 2D vector containing x_q and y_q is rewritten in terms of homogeneous coordinates, making it a projective element: $\mathbf{Q} = [x_q, y_q, 1]$. The 3D vector is also written this way: $\mathbf{P} = [X_p, Y_p, Z_p, 1]$. Furthermore, instead of the equality, proportionality is assumed [5]:

$$\begin{pmatrix} x_q \\ y_q \\ 1 \end{pmatrix} \propto \begin{pmatrix} f_x & s & x_r & 0 \\ 0 & f_y & y_r & 0 \\ 0 & 0 & 1 & 0 \end{pmatrix} \begin{pmatrix} X_p \\ Y_p \\ Z_p \\ 1 \end{pmatrix} \quad (5)$$

In vector notation, this becomes:

$$\mathbf{Q}_i \propto \mathbf{K}_i (\mathbf{I} \mid \mathbf{0}) \mathbf{P}_i \quad (6)$$

Since, the derivation of the pinhole camera model can be applied to both a camera and projector, the subscript i can either be c or p , representing the camera or projector respectively. In this equation, \mathbf{K}_i is the camera or projectors intrinsic matrix:

$$\mathbf{K}_i = \begin{pmatrix} f_{x,i} & s_i & x_{r,i} \\ 0 & f_{y,i} & y_{r,i} \\ 0 & 0 & 1 \end{pmatrix} \quad (7)$$

2.1.3 Distortion

The pinhole model describes the camera as an ideal image capturing device by assuming an infinitesimal aperture and a distortion-free objective lens. For most cameras, especially with wide-angle lenses, the latter is almost never the case resulting in deviations from the pinhole model. Several nonlinear distortions are introduced in almost all lenses, of which radial distortion, illustrated in figure 4, is the most severe part [5].

Let $\mathbf{Q} = [x_q, y_q]$ be the ideal, distortion-free camera pixel coordinates and $\tilde{\mathbf{Q}} = [\tilde{x}_q, \tilde{y}_q]$ the real observed distorted pixel coordinates. The radial distortion can be estimated using the division model [11]:

$$\mathbf{Q} = \frac{1}{L(r)} \tilde{\mathbf{Q}} + \left(1 - \frac{1}{L(r)}\right) \mathbf{D} \quad (8)$$

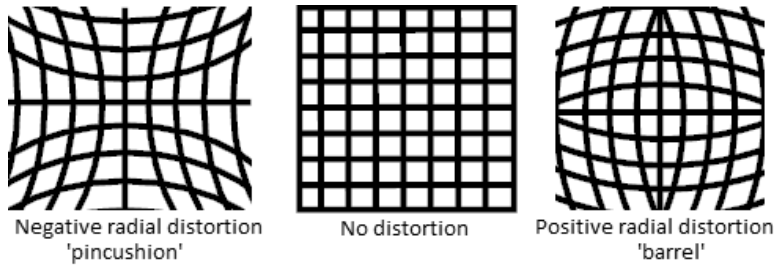


Figure 4: Radial distortion[14]

In this equation, $\mathbf{D} = [x_d, y_d]$ is the distortion center, which can be assumed to be the principal point: $\mathbf{D} = \mathbf{R} = [x_r, y_r]$. Furthermore, $L(r)$ is the distortion factor, which only depends on the distance from the distortion center, r :

$$r = \sqrt{(x_q - x_d)^2 + (y_q - y_d)^2} \quad (9)$$

The function $L(r)$ is only defined for positive values of r and can be approximated by a Taylor expansion:

$$L(r) = 1 + k_1 r^2 + k_2 r^4 + k_3 r^6 \dots \quad (10)$$

Where k_n are the radial distortion coefficients, of which often only one or two terms need to be determined for sufficient accuracy.

2.1.4 Field of view

The field of view (FOV) of the camera is an important measure for the minimum measurement range of a camera based measurement system since scenic points that are located outside the FOV are, by definition, not seen by the camera. The FOV is determined by the dimensions of the image sensor, N_x and N_y , expressed in pixels, and the focal length f of the camera. Strictly speaking there is a difference in the horizontal and vertical field of views. In this case however, the FOV is regarded as the smallest of the two. Assuming $N_x > N_y$, the FOV, ν in radians is given by[5]:

$$\nu = \arctan\left(\frac{N_y}{2f_y}\right) \quad (11)$$

2.2 Active Stereo Vision

2.2.1 Coordinate transformation

A point \mathbf{P} in the camera's and projector's coordinate frame, Ψ_c and Ψ_p can be related using a homogeneous coordinate transformation[5]:

$$\mathbf{P}_p = \left(\mathbf{R}_c^p \mid \mathbf{t}_c^p \right) \mathbf{P}_c \quad (12)$$

Where the rotation matrix $\mathbf{R}_{\mathbf{c}}^{\mathbf{P}}$ and the translation vector $\mathbf{t}_{\mathbf{c}}^{\mathbf{P}}$ are the extrinsic parameters of the ASV system. The rotation matrix represent the orientation of the coordinate frames and can be decomposed and written in terms of the angle of rotation around the x-,y- and z-axis axis:

$$\mathbf{R}_{\mathbf{c}}^{\mathbf{P}}(\alpha, \beta, \zeta) = \mathbf{R}_{\mathbf{c},\mathbf{x}}^{\mathbf{P}}(\alpha)\mathbf{R}_{\mathbf{c},\mathbf{y}}^{\mathbf{P}}(\beta)\mathbf{R}_{\mathbf{c},\mathbf{z}}^{\mathbf{P}}(\zeta) \quad (13)$$

$$\mathbf{R}_{\mathbf{c},\mathbf{x}}^{\mathbf{P}}(\alpha) = \begin{pmatrix} 1 & 0 & 0 \\ 0 & \cos\alpha & \sin\alpha \\ 0 & -\sin\alpha & \cos\alpha \end{pmatrix} \quad (14)$$

$$\mathbf{R}_{\mathbf{c},\mathbf{y}}^{\mathbf{P}}(\beta) = \begin{pmatrix} \cos\beta & 0 & -\sin\beta \\ 0 & 1 & 0 \\ \sin\beta & 0 & \cos\beta \end{pmatrix} \quad (15)$$

$$\mathbf{R}_{\mathbf{c},\mathbf{z}}^{\mathbf{P}}(\zeta) = \begin{pmatrix} \cos\zeta & \sin\zeta & 0 \\ -\sin\zeta & \cos\zeta & 0 \\ 0 & 0 & 1 \end{pmatrix} \quad (16)$$

Furthermore, the translation vector, $\mathbf{t}_{\mathbf{c}}^{\mathbf{P}}$ can be decomposed into:

$$\mathbf{t}_{\mathbf{c}}^{\mathbf{P}} = \begin{pmatrix} t_x \\ t_y \\ t_z \end{pmatrix} \quad (17)$$

Combining equation 6 and 12 results in[5]:

$$\begin{aligned} \mathbf{Q}_{\mathbf{c}} &\propto K_c (\mathbf{I} \mid \mathbf{0}) \mathbf{P}_{\mathbf{c}} \\ \mathbf{Q}_{\mathbf{p}} &\propto K_p (\mathbf{R}_{\mathbf{c}}^{\mathbf{P}} \mid \mathbf{t}_{\mathbf{c}}^{\mathbf{P}}) \mathbf{P}_{\mathbf{c}} \end{aligned} \quad (18)$$

Note that it was assumed that the z-axis was aligned with the camera's optical axis, and thus $\zeta = 0$.

2.2.2 Optical Triangulation

Point $\mathbf{P}_{\mathbf{c}} \in \mathbb{R}^3$ defines two corresponding points $\mathbf{Q}_{\mathbf{c}}$ and $\mathbf{Q}_{\mathbf{p}}$ in the camera's and projector's image planes, ψ_c and ψ_p . These three points, or equivalently $\mathbf{P}_{\mathbf{c}}$, $\mathbf{O}_{\mathbf{c}}$ and $\mathbf{O}_{\mathbf{p}}$, define a triangle that is fully determined by the point correspondences and the intrinsic and extrinsic parameters of the ASV system. As the triangle is known, the 3D coordinates of the point can be calculated. For an arbitrary projection pattern, it follows from equation 18 and that each pair of corresponding points $\mathbf{Q}_{\mathbf{c}}$ and $\mathbf{Q}_{\mathbf{p}}$ defines four equations on \mathbf{P} and can be solved for if the intrinsic and extrinsic parameters of the ASV system are known. This is done using a direct linear transformation algorithm (DLT algorithm). This DLT problem arises from the proportionality that is assumed in equation 6. Without going too much into detail, a homography can be estimated, which imposes constraints on the intrinsic parameters[12].

The resulting equation takes pairs of points, $(\mathbf{Q}_c, \mathbf{Q}_p)$ as an input and has as output a scaled version of the image point: $\lambda \mathbf{P}$. In this equation, λ is any real number, which can be calibrated for.

A common problem for any stereo vision systems is to find these point correspondences. Using epipolar geometry, a constraint can be imposed on the location of \mathbf{Q}_c , if \mathbf{Q}_p is known, or vice versa.

2.2.3 Epipolar Geometry

Three points, \mathbf{O}_c , \mathbf{O}_p and \mathbf{P} define a plane ψ_e , called the epipolar plane, in which \mathbf{Q}_c and \mathbf{Q}_p are also located. The line $\mathbf{O}_c\mathbf{O}_p$ is called the triangulation base and its length the base distance. This line intersects the image planes ψ_c and ψ_p in \mathbf{e}_c and \mathbf{e}_p respectively. These points are called the epipoles and the lines $\mathbf{e}_c\mathbf{Q}_c$ and $\mathbf{e}_p\mathbf{Q}_p$ the epipolar lines. This geometry is illustrated in figure 5[5].

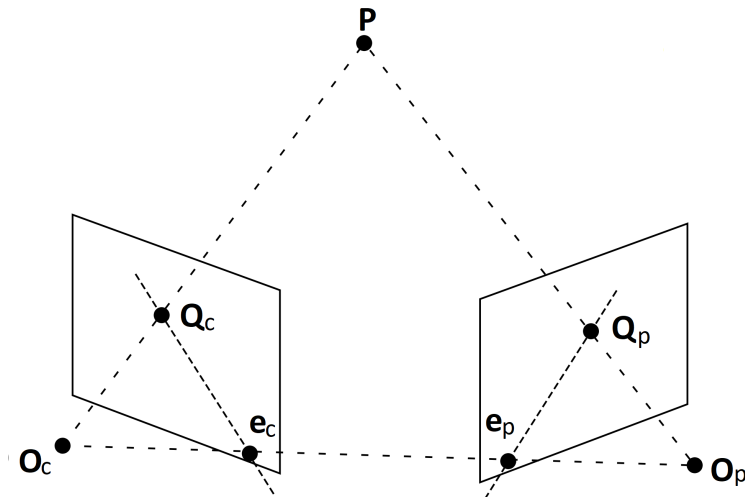


Figure 5: Epipolar geometry[5]

The epipolar geometry is the intrinsic projective geometry between two views. It is independent of scene structure, and only depends on the camera and projectors internal parameters and relative pose. The constraint that arises from this geometry is encapsulated by the fundamental matrix \mathbf{F} . If point \mathbf{P} is imaged as \mathbf{Q}_c in the first view, and \mathbf{Q}_p in the second, then the image points satisfy the relation:[5]

$$\mathbf{Q}_p^T \mathbf{F} \mathbf{Q}_c = 0 \quad (19)$$

Equation 18, combined with the equation above results in:

$$\mathbf{F} = \mathbf{K}_p^{-T} (\mathbf{t}_c^p \times \mathbf{R}_c^p) \mathbf{K}_c^{-1} \quad (20)$$

This equation states that for any \mathbf{Q}_p , its corresponding points \mathbf{Q}_c is located on the epipolar line $\mathbf{e}_p \mathbf{O}_p$.

2.3 Configurations

In this analysis, the projected pattern is assumed to either be a cone, or be bounded by a cone. This shape is parametrized in terms of u , θ and the half fan angle ϕ , or written in implicit form as:

$$\mathbf{J} = \begin{pmatrix} J_1 \\ J_2 \\ J_3 \end{pmatrix} = \begin{pmatrix} u \tan(\phi) \cos(\theta) \\ u \tan(\phi) \sin(\theta) \\ u \end{pmatrix} \quad (21)$$

$$J_1^2 + J_2^2 - (J_3 \tan(\phi))^2 = 0$$

A variety of configurations of the camera and cone projector are possible and in principle they can all be used for the pipe profiling system, as long as the projected light pattern is in the FOV of the camera. However, since the system has to detect obstacles that are in front of the robot, the optical axes of camera and projector should be oriented in the same direction. The remaining configurations can be subdivided according to the position of the epipole \mathbf{e}_p in the projector plane:[5]

1. The epipole \mathbf{e}_p is located within the projected shape, defined by 21. In this case there is exactly one point correspondence \mathbf{Q}_c for any \mathbf{Q}_p and consequently there is a one-to-one correspondence between any point in the camera plane and a point on the laser cone.
2. The epipole \mathbf{e}_p is located outside the projected shape. In this case there are at maximum two point correspondences \mathbf{Q}_c for any \mathbf{Q}_p so ambiguities exist when reconstructing the scenic point.
3. The epipole \mathbf{e}_p is located on the projected shape. In this case there are an infinite number of point correspondences for \mathbf{Q}_c associated with $\mathbf{Q}_p = \mathbf{e}_p$. This is an undesired situation and should be prevented.

2.3.1 Configuration I

In this configuration, the optical axes of the camera and projector coincide, such that the extrinsic parameters can be written as:

$$\mathbf{R}_c^p = \mathbf{I} \quad (22)$$

$$\mathbf{t}_c^p = (0, 0, t_z) \quad (23)$$

In this configuration, which is visualized in figure 6 and 7, the epipoles \mathbf{e}_c and \mathbf{e}_p are located in their associated principal points and the epipolar lines are radially symmetric around these principal points, $(\mathbf{x}_r, \mathbf{y}_r)$. This

symmetry allows for simplified equations for reconstructing point \mathbf{P}_c , which can be solved uniquely under the condition $Z_c > 0$. We start by defining the following parameters:

$$r_c = \sqrt{(x_{q,c} - x_{r,c})^2 + (y_{q,c} - y_{r,c})^2} \quad (24)$$

$$r_p = \sqrt{(x_{q,p} - x_{r,p})^2 + (y_{q,p} - y_{r,p})^2} \quad (25)$$

$$R_p = \sqrt{X_p^2 + Y_p^2} \quad (26)$$

By rearranging, these equations can be written as:[5]

$$R_p = \frac{Z_p}{f_c} r_c \quad (27)$$

$$Z_p = \frac{r_p t_z}{r_c - r_p} \quad (28)$$

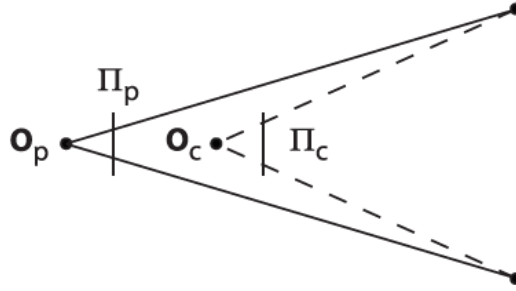


Figure 6: Geometry of configuration I[5]

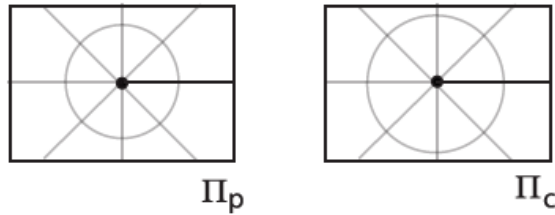


Figure 7: Epipolar geometry of configuration I[5]

Having a radially symmetric system, allows for the measurements to also to radially symmetric. This means that points \mathbf{P}_c at equal distance from the optical axes, can be reconstructed with equal accuracy. This is a favorable property, especially for pipe inspection, since most of the pipe can be considered radially symmetric. This means that if the ASV system is near

the center of the pipe, the pipe’s surface will be reconstructed with equal accuracy everywhere.

A more practical advantage of this configuration, is that optical aiding devices, such as lenses, can be shared by the camera and projector, since their optical axes coincide. The main disadvantage of this configuration is the added challenge of making sure the camera and projector do not block each others sight.

2.3.2 Configuration II

In this configuration, the optical axes of the camera and projector are parallel to each other, such that the extrinsic parameters of the ASV system can be written as:

$$\mathbf{R}_c^p = \mathbf{I} \quad (29)$$

$$\mathbf{t}_c^t = (t_x, 0, 0) \quad (30)$$

In this configuration, the epipoles are located at infinity and the epipolar lines are collinear and parallel to the horizontal axes of the camera and projector image planes. A visualization of this configuration and epipolar geometry is found in figure 8 and 9. The simplified equations for reconstruction of a point \mathbf{P}_c are given by:[5]

$$X_p = \frac{Z_p}{f_c}(x_{q,c} - x_{r,c}) \quad (31)$$

$$Y_p = \frac{Z_p}{f_c}(y_{q,c} - y_{r,c}) \quad (32)$$

$$Z_p = \frac{f_c t_x}{x_{q,p} - x_{q,c}} \quad (33)$$

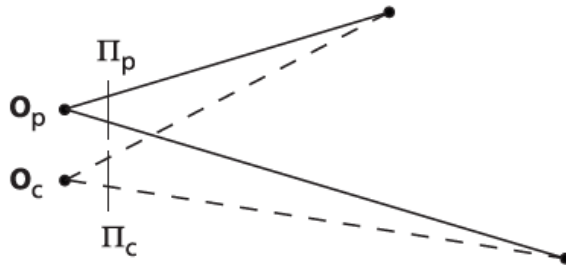


Figure 8: Geometry of configuration II[5]

As mentioned before, each epipolar line intersects the projection circle twice. This correspondence problem can be solved by assuming the relative ordering of pixels is the same in the camera and projector’s image planes. Since this configuration lacks radial symmetry, the pipe’s surface will be

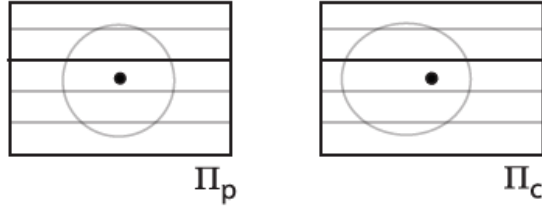


Figure 9: Epipolar geometry of configuration II[5]

reconstructed with unequal accuracy. Furthermore, if the projector is not in the center of the pipe, the laser curve will be spread out over the pipe's surface. This means its thickness increases, its relative peak intensity decreases and the range of values Z_c increases. Combining this with the limited depth of focus of the image capturing device results in unsharp images and thus less accurate curve extraction. This is especially true when capturing images at short range.

2.4 Measurement Range

The measurements range of the ASV system is a direct result of the configuration and geometry. In case of configuration I, it depends on the base distance t_z , half fan angle, ϕ and field of view of the camera, ν . If the camera is placed in front of the projector, $t_z > 0$, a minimum distance can be defined under the assumption $\phi > \nu$. If the projector is placed in front of the camera, $t_z < 0$, a maximum distance can be defined when assuming $\phi < \nu$. In a later section will be shows that the resolution of the system is enhanced when $t_z > 0$ and thus a minimum measurement range can be defined as:[5]

$$R_{c,min} = \frac{\tan \phi \tan \nu}{\tan \nu - \tan \phi} t_z \quad (34)$$

$$Z_{c,min} = \frac{R_{c,min}}{\tan \phi} - t_z \quad (35)$$

While the maximum distances to be measured are in theory infinite, in practice it is limited by the amount of light captured by the image sensor. This depends on the power of the laser, the reflectivity of the pipes surface and the sensitivity of the image sensor.

3 Analysis

3.1 Error analysis

This section aims to analyze the errors when reconstructing \mathbf{P}_c , when the ASV system is in the radially symmetric configuration. The largest errors are due to the sampling of pixels and calibration of the internal and external ASV parameter. The equations from section 2.3.1 are repeated, with $r_p = f_c \tan(\phi)$:

$$R_p = \frac{Z_c}{f_c} r_c \quad (36)$$

$$Z_p = \frac{f_c \tan(\phi) t_z}{r_c - f_c \tan(\phi)} \quad (37)$$

The errors in this case are the absolute errors on the coordinates, which have been propagated from errors in r_c , f_c , ϕ and t_z . The calculation for the statistical, absolute error in a function, $F(\mathbf{a})$ with respect to a parameter $a_i \in \mathbf{a}$ uses the partial derivatives of F , multiplied by the absolute error in a_i . The combined effect of these errors in \mathbf{a} is expressed as the Root-Sum-Square, leading to the final expression:

$$\Delta F_{a_i} = \frac{\delta F}{\delta a_i} \Delta a_i \quad (38)$$

$$\Delta F(\mathbf{a}) = \sqrt{\sum_{i=1} (\Delta F_{a_i})^2} \quad (39)$$

3.1.1 Sampling error

Sampling errors are the errors due to spatial image quantization that occurs in the camera. These errors are at most half a pixel in both x and y direction. However, since the the laser curve is extracted with sub pixel accuracy, the sampling errors can be assumed to be less than half a pixel. The parameter that suffers from quantization is r_c :

$$\Delta R_{c,r_c} = \left| \frac{(R_c - t_z \tan(\phi))^2}{f_c t_z \tan^2(\phi)} \right| \Delta r_c \quad (40)$$

$$\Delta Z_{c,r_c} = \left| \frac{Z_c^2}{f_c t_z \tan(\phi)} \right| \Delta r_c \quad (41)$$

From the first equation is it observed that the error, $\Delta R_{c,r_c}$, is smallest when $t_z < 0$. This confirms that in the configuration where the optical axes of the camera and projector coincide, the error is smallest if the camera is in front. Furthermore, increasing ϕ , f_c or t_z will decrease the absolute error.

3.1.2 Calibration error

Calibration errors arise due to uncertainties in the geometry of the system. The specific parameters are f_c , $\tan(\phi)$ and t_z . The errors are given by:

$$\Delta R_{c,f_c} = \left| \frac{R_c(R_c - t_z \tan(\phi))}{f_c t_z \tan(\phi)} \right| \Delta f_c \quad (42)$$

$$\Delta Z_{c,f_c} = \left| \frac{Z_c(Z_c + t_z)}{f_c t_z} \right| \Delta f_c \quad (43)$$

$$\Delta R_{c,\tan(\phi)} = \left| \frac{R_c^2}{t_z \tan^2(\phi)} \right| \Delta \tan(\phi) \quad (44)$$

$$\Delta Z_{c,\tan(\phi)} = \left| \frac{Z_c(Z_c + t_z)}{t_z \tan(\phi)} \right| \Delta \tan(\phi) \quad (45)$$

$$\Delta R_{c,t_z} = \left| \frac{R_c}{t_z} \right| \Delta t_z \quad (46)$$

$$\Delta Z_{c,t_z} = \left| \frac{Z_c}{t_z} \right| \Delta t_z \quad (47)$$

The chain rule is used to obtain the error, $\Delta \tan(\phi)$:

$$\Delta \tan(\phi) = (1 + \tan^2(\phi)) \Delta \phi \quad (48)$$

3.2 System calibration

This section describes the calibration procedure that is used to obtain the intrinsic and extrinsic parameters of the ASV system that are needed to reconstruct points in 3D space. The procedure is flexible and does not require expensive equipment as it only makes use of a so-called model plane containing well defined feature points.

3.2.1 Camera matrix

In the first step, the camera is calibrated to find \mathbf{K}_c , using the Matlab toolbox developed by Jean-Yves Bouguet. The procedure requires a series of calibration images, which is simply an image of a model plane with a checkerboard pattern. To extract the feature points in the calibration images, a refined Harris corner detector is present in the toolbox. It is capable of detecting the corners of the checkerboard pattern with sub-pixel accuracy. The feature points and their projections in the camera plane are used to estimate a so-called homography that imposes constraints on the camera's intrinsic parameters. The entire procedure can be summarized as follows:

1. Take a series of pictures of the chessboard-patterned model plane, at different distances and angles from the plane.

2. Initialize the corner extraction algorithm by clicking on the four extreme corners on the rectangular checkerboard pattern.
3. Specify the sizes of the checkerboard rectangles on the model plane, dX and dY in mm.
4. After the corner extraction, calibration is performed in two steps: initialization and nonlinear optimization. The initialization step computes a closed-form solution for the calibration parameters based not including any lens distortion. The non-linear optimization step minimizes the total reprojection error, using least squares, over all the calibration parameters. These are 9 intrinsic parameters ($f_{x,c}$, $f_{y,c}$, $x_{r,c}$, $y_{r,c}$ and 5 distortion coefficients) and $6*N$ extrinsic parameters, where N is the number of calibration images. Note that the skewness is assumed to be zero. The optimization is done by iterative gradient descent with an explicit computation of the Jacobian matrix.
5. Recompute the image corners on all images automatically, by using the reprojected grid as initial guess locations, as opposed to clicking manually.
6. Perform another calibration procedure, this time without initialization.
7. Inspect the plot of the reprojection error and select images in which corner detection was relatively unsuccessful. Either repeat step 5 and 6 on the selected images, with different window sizes, or suppress the images from the calibration performed in step 6.

3.2.2 Extrinsic ASV parameters

In the second step, the projector is calibrated to find \mathbf{R}_c^P and \mathbf{t}_c^P . This procedure uses a model plane that can be translated in the z-direction and tilted along the two axis that constituent the plane. Furthermore, the model plane should contain a removable checkerboard pattern.

1. The model plane with checkerboard pattern is placed in front of the stationary ASV system, such that it is entirely in the field of view of both the camera and projector. The Matlab toolbox that is used for calibrating the camera, is used to obtain the camera's translation and rotation with respect to the model plane. Either the plane or ASV system are moved until the camera's image plane and the model plane are parallel to each other.
2. Now the checkerboard pattern is removed, and a cone is projected. This will result in an off-center ellipse on the model plane. An algorithm analyses the image captured by the camera, finds the projected shape and determines the ratio of minor and major diameter.

3. The angles of projector with respect to the camera are adjusted and the previous step is repeated until the minor and major diameter are equal, meaning the projector's image plane and the model plane are aligned parallel to each other and a circle is projected.
4. In this step the projector is translated with respect to the camera, such that the center of the projected circle falls onto the principal point in the image plane of the camera. After this step, the projector's coordinate transformation with respect the to the camera is merely a translation in the z-direction: $\mathbf{R}_m^P(0, 0, 0)$ and $\mathbf{t}_m^P = (0, 0, t_z)$.

3.2.3 Projector Matrix and t_z

Similarly to the camera's matrix, the skewness is assumed to be zero. This leaves five parameters ($f_{x,p}$, $f_{y,p}$, $x_{r,p}$, $y_{r,p}$ and t_z) and an arbitrary amount of distortion coefficients.

For this final step, the procedure above has to be followed, such that the camera's image plane, projector's image plane and model plane are all parallel and differ by a translation t_z . In this configuration, the height and width, H and W, of the image on the model plane are measured using a ruler, together with the distance between the model plane and projector, D. The distance between the focal point of the projector and model plane is D + E, where e is a positive constant, since the focal point can be assumed to be 'inside' the projector. The focal lengths $f_{x,p}$ and $f_{y,p}$ are calculated by:

$$f_x = \frac{x_q}{W}D + \frac{x_q}{W}E \quad (49)$$

$$f_y = \frac{y_q}{H}D + \frac{y_q}{H}E \quad (50)$$

By taking measurements of H and W at several distances D, E can be estimated using a linear mean square fit, and the focal lengths follow from that calculation.

Furthermore, at every distance D, the Matlab toolbox is used to calculate the distance between the camera and model plane, G. This allows for a calculation of t_z via:

$$t_z = (D + E) - G \quad (51)$$

$x_{r,p}$ and $y_{r,p}$ are estimated to be equal to half the resolution of the projector in x and y direction respectively.

Lastly, the radial distortion coefficients are determined by projecting a checkerboard pattern on the model plane, taking an image with the camera and using the Matlab toolbox. The distortion of the projector is simply the distortion in the image, minus the camera's distortion.

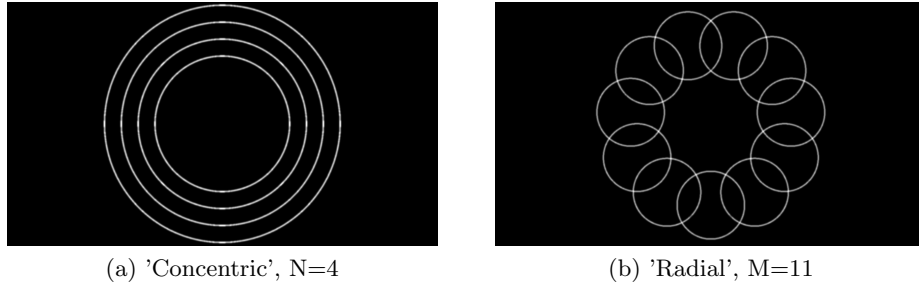


Figure 10: Examples of the two types of patterns

3.3 Patterns

The patterns that are investigated all use cones as basic building blocks, since these are possible to project using a laser as demonstrated in [6].

A projection of a cone on a parallel surface will result in a circle, while it will show an ellipse on a surface at an angle. The ratio of radii in this ellipse will provide information on the angle of the surface, making projections of cones suitable for the purpose of pipe inspection.

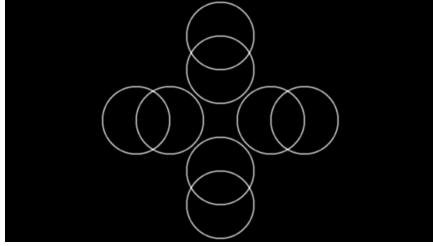
Furthermore, using only cones allows each pattern to be compared to an ordinary cone, by defining the complexity of a pattern as the number of cones. The best pattern will have the highest ratio of results to complexity when comparing the pattern with the ordinary cone.

While the laser patterns are 3 dimensional and consisting of cones, the analysis is simplified by defining 'patterns' as 2D images that consist of circles. There are two main methods of creating patterns from circles: a) moving the center of the circle with respect to the center of the image, b) change the radius of the circle with respect to the smallest dimension of the image. The two extreme's that arise from these methods are concentric circles and circles whose centers lie on a circle, dubbed 'concentric' and 'radial' type patterns from here on. Examples of these extreme's are given in figure 10. Combinations of these patterns are also possible, as exemplified in figure 11.

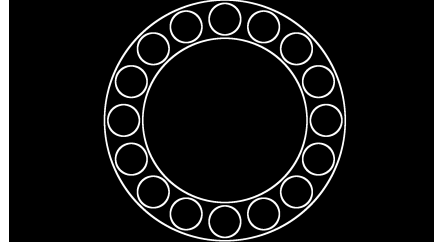
3.3.1 Generating patterns

The images that will be used for testing have been produced as follows:

1. Distance- and image-array with dimensions equal to the number of pixels, (i,j) are initialized. Multiple distance-array are generated, one for every circle in the pattern. The variable 'n' keeps track of the different circles are corresponding distance-arrays.
2. The shape that is to be projected is written in parametric form:



(a) Combination of 'concentric' and 'radial', $N=2$, $M=4$



(b) Combination of 'concentric' and 'radial', $N=2$, $M = 11$

Figure 11: Examples of combinations of the two types of patterns

$$\begin{aligned}x &= x_center + r * \cos(\theta) \\y &= y_center + r * \sin(\theta)\end{aligned}$$

3. For each element in a distance-array, the geometric distance to the parametrically defined pattern is calculated using the implicit form of the equation for a circle:

$$\text{distanceArray}(i, j, n) = |((i-x_center(n))^2 + (j-y_center(n))^2) - r(n)^2|$$

4. The distance arrays are then combined into an image array using a margin:

```
for (n = 1:N)
    if (distanceArray(i, j, n) < margin)
        imageArray(i, j) = 1
    end
end
```

5. A normal distribution with a certain standard deviation and a mean of zero is applied to simulate best the intensity distribution of a laser.
6. The array is normalized, such that the brightest pixel has an intensity of 255.

3.3.2 Parameters of patterns

The parameters of these patterns can be divided into two categories; parameters that define the shape, and parameters that determine how this shape is visualized. The aim is to investigate the first, independently of the second. The parameters that influence the visualization are the margin that defines the initial line thickness and the standard deviation of the Gaussian filter. These are chosen so they are comparable to a laser curve and remain constant.

The other parameters include the radius and center of the circle(s) and the

number of circles. Especially the pattern using features of both of the other patterns have a lot of possible configurations. Therefore, test are initially done using both concentric and radially aligned cones independently. Based on the results, combinations of both types are created that best fit their strengths and weaknesses.

3.3.3 Colors of patterns

While one end of the pipe was closed off with a light blocking element, the other side was still open during measurements. This allowed for light to enter and add noise to the measurements. The reflections of the pattern on the inner pipe wall further decreased the contrast. In order to better simulate the conditions the PIRATE robot would be in, the color that would reflect least was chosen to perform measurements with. Several patterns were generated in white, red, green and blue and projected into the pipe. Table 1 list the average intensities (between 0 and 255) of the grayscale image taken by the camera for every color. From this, it was concluded that blue was the least reflective for this pipe, making it most suitable for reproducing laser light.

Table 1: Average intensities of grayscale images for different projected colors

Color	White	Red	Green	Blue
Average intensity	39.1	23.7	30.3	12.0

3.4 Image processing

The image processing steps that are needed to extract the useful information from the images captured by the camera in the ASV system are the topic of this section. The measurement image is defined as a matrix with the same dimensions as the amount of pixels in the imaging sensor. The elements of this matrix represent the grayscale values of the pixels, between 0 and 255. To extract the location of the laser curve in the image, some basic image processing steps are required. Furthermore, some specialized functions are required that depend on the projected pattern.

It is noted that these steps have not been optimized in order to be performed in real-time. When the location of the points of interest in the image have been determined, equation 27 and 28 are used to calculate the position of the curve in \mathbb{R}^3 , with respect to the camera. The steps can be summarized as follows:

1. Undistortion: Correct for radial distortion caused by lens
2. Median filter: Smooth out noise
3. Threshold: Remove noise

4. Object selection: Isolate curve from pipe wall. This step has multiple versions, that depend on what pattern is used and what feature of the reflection is to be analyzed
5. Dilation: Smooth out thresholding gaps
6. Intensity adjustment: Increase contrast
7. Polar transformation
8. Intensity weighted fit: Fit a curve to the data
9. Reconstruction in \mathbb{R}^3 : Reconstruct position of laser curve

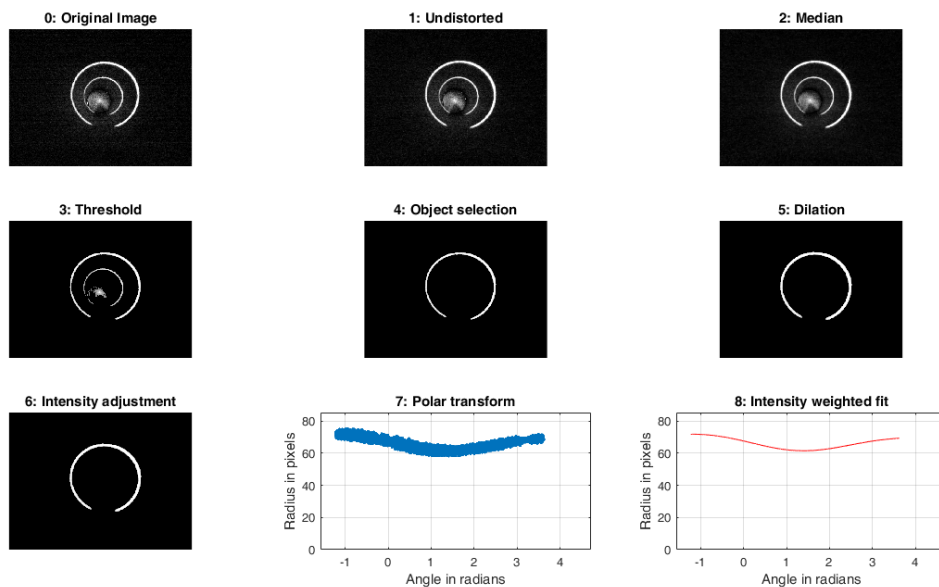


Figure 12: Example of image processing steps 1-8

Figure 12 shows an example of the first 8 steps. Figure 13 shows step 9 after the data from step 8 has been combined for the objects of interest.

3.4.1 Undistortion

The image's radial distortion is removed, using the radial distortion coefficients and the camera matrix as parameters.

3.4.2 Median filter

In this preprocessing step, the image is altered using a non-linear digital filter, called a median filter. The goal is to remove so called 'salt-and-pepper' noise, while preserving the general shape and edges. This filter

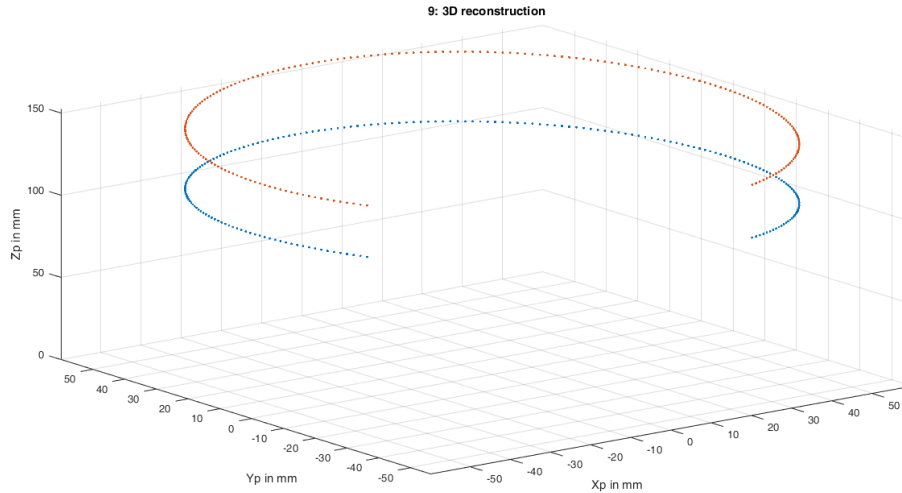


Figure 13: Example of image processing step 9

replaces each entry with the median of neighboring entries. When using a square 'window' that encapsulates an odd number of entries, the median can easily be found by listing the entries in numerical order and taking the middle number. This step requires a window size as an input, for which the minimum of 3 by 3 is chosen.

3.4.3 Threshold

In thresholding, an entry is replaced with a zero if it is below a certain value, the threshold. The goal is to remove the noise that was 'smoothed out' by the median filter, but also reflections of the laser that are not of interest. This step requires a threshold value 'T' for each concentric circle that has to be detected.

3.4.4 Object selection

This step consists two parts. The first part, which is applied to every image, has as output a list of non-touching objects that are in the image and their properties. In the second part, specific features are extracted from these objects and put into a list that represents the information that is extracted from the image.

In the first step, connected-component labeling is used on a binarized version of the image to find the number of non-touching objects and their properties. The algorithm assigns a temporary label to each pixel, based on the pixels in the neighborhood. This way, each pixel gets labeled 'background' or a temporary new label. In the second pass, touching labels are deemed equal and each pixel is assigned the lowest label which is equal to their own.

The only parameter of this step is the 'connectivity', which is comparable to a window size.

The output of connected-component labeling are groups of pixels, representing connected objects in the image. Some useful properties of these objects are:

- Area: The area of an object is defined as the amount of pixels in an object.
- Bounding box: The smallest rectangle that can be draw, such that the objects fits inside. This is determined by taking the minimum and maximum of an objects x and y coordinates.
- Area ratio: This is defined as the ratio between the area of the object and the area of the smallest rectangle that fits around the object.
- Location: The location the object's center of mass
- Average intensity: This is determined by adding the intensity of all pixels that are part of an object and dividing by the area.

Using these properties, objects are identified as follows:

- Objects with small areas are considered noise.
- Objects near the center of the image with large area ratios and low average intensities are considered reflections.
- The remaining object or objects are considered to be the laser curve.

The second step depends on the type of pattern that is being analyzed and what feature is of interest. Table 2 gives the type of pattern that is analyzed, the feature of interest, a brief explanation of the steps involved and a reference to an example.

Table 2: Methods for selecting specific features in selected objects

Pattern	Feature	Example	Explanation
Concentric	-	12	No further feature selection
Radial	Intersections	14	First the object is skeletonized. Second, the object is cleaned up by removing the endpoints of the smallest branches. Lastly, the remaining banchpoints are saved, which represent the location where two circles intersect.
Radial	Min/Max	15	For each of the initially selected objects, the points closest and further from the image center are saved into a list. Curves are fitted to the list of points closest and to the list of points furthest to the image center.
Radial	Half-circles	16	First, the bounding box of the object is used to calculate the center of the object. Second, every point's distance to the image center is calculated. If this distance is shorter than the distance between the objects center and the image center, it is discarded.

3.4.5 Dilation

The pattern projected by the laser and captured by the camera often contains many small unwanted gaps. The basic effect of dilation is to enlarge the boundaries of regions of foreground pixels. Thus areas of foreground pixels grow in size while holes within those regions become smaller.

3.4.6 Intensity adjustment

In this step, the intensity of pixels is increased, such that the brightest pixel has a value of 1.

3.4.7 Polar transform

If the pixel coordinates are taken as Cartesian coordinates, each value would lie in the positive x, positive y plane. Therefore, the image is shifted by $-x_{r,c}$, $-y_{r,c}$ in the x and y direction respectively, to obtain the correct position to

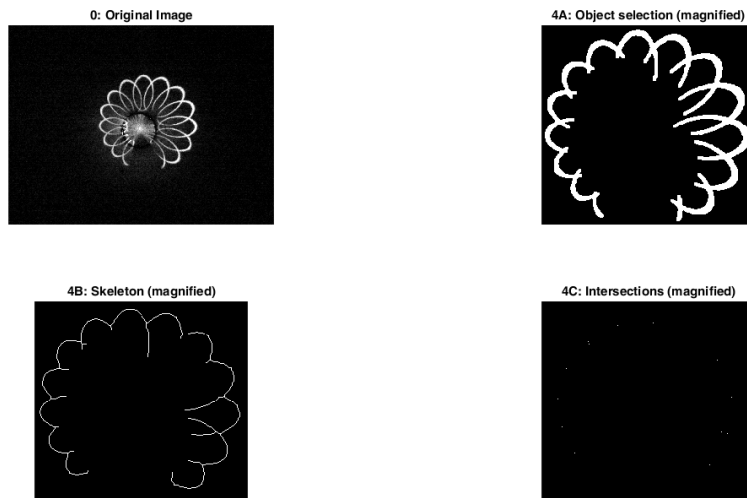


Figure 14: Example of image processing step 4: 'Intersections'

apply the polar transformation. This transformation is given by[15]:

$$\theta = \text{atan2}(y, x) \quad (52)$$

$$\rho = \sqrt{x^2 + y^2} \quad (53)$$

In this equation, θ and ρ are the polar coordinates and atan is a common variation on the arctangent function.

3.4.8 Intensity weighted fit

In order to refine the extracted laser curve, the central thread of the curve has to be found. For this purpose, it is assumed that the intensity of the captured laser curve is Gaussian distributed in the radial direction and a simple method of refining the curve would be to consider the brightest pixel in the radial direction as the center of the curve. Note however, that because of image formation and processing properties, the real distribution will not be Gaussian; quantization, saturation and thresholding result in a 'deformed' Gaussian distribution and a more reliable way of refinement is to take all laser curve pixels in a radial segment into consideration. A robust and reliable method is to take the intensity weighted average of the pixel radii as the central thread of the laser curve.

Several types of fits have been tested: First order Fourier, Second order Fourier, Third order polynomial, Fifth order polynomial and Cubic spline. In each fit, the pixel intensity is used as a weight for the corresponding polar coordinate.

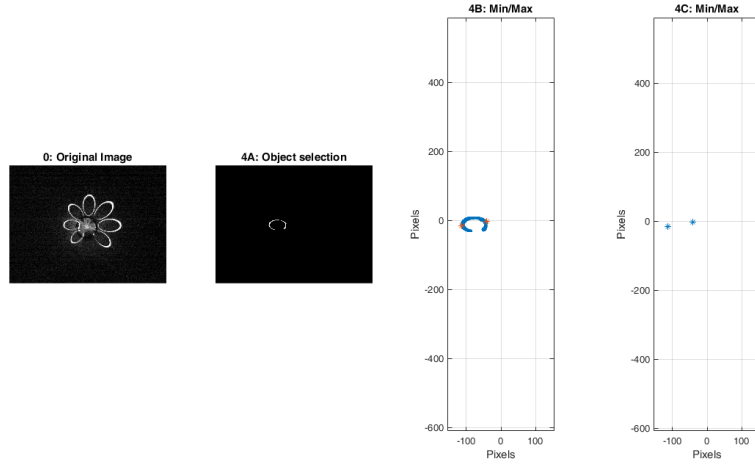


Figure 15: Example of image processing step 4: 'Min/Max'

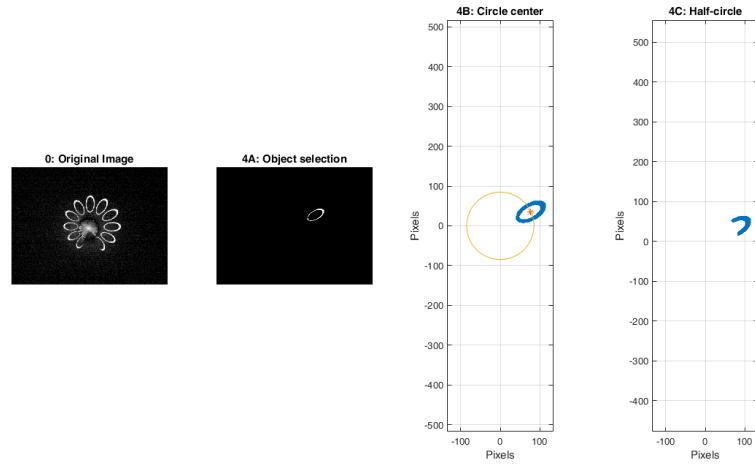


Figure 16: Example of image processing step 4: 'Half-circles'

3.4.9 Reconstruction

In this final step, equation 27 and 28 are applied to reconstruct the position of the laser curve with respect to the camera in \mathbb{R}^3 . Since proportionality was assumed in equation 6, the calculated coordinates have to be multiplied by a scalar to find the real coordinate. Since the pipe diameter is known, X_p and Y_p can easily be scaled to the proper value in millimeters. In order to scale Z_p correctly, an extra calibration procedure would be required in which a ruler is used to measure the distance between the camera and location where the projected pattern hits the pipe wall. Because this procedure was not performed, Z_p has been normalized. Lastly, the equations given in 3.1 are used to calculate the corresponding error.

4 Design

4.1 Equipment

Instead of creating a setup with lasers for every pattern, a projector is used, namely the Optoma Pico-PK120. The ELP-USBFHD06H-L36 USB camera is chosen to be the camera in this ASV setup, mainly due to its wide-angle lens and easy of use.

4.2 Measurement structure

A structure is designed in SolidWorks and lasercut out of Delrin to hold both the projector and camera in their desired orientation; $\mathbf{R}_c^p = \mathbf{I}$, $\mathbf{t}_c^p = (0, 0, t_z)$. All pieces have a thickness of 2 mm, unless stated otherwise. It has been designed such that it allows for slight changes from the ideal configuration, which allows the effects of mis-calibration to be investigated.

A set of technical drawings can be found in the appendix, 7.2. The design features a long stick (5 mm thick), which is strengthened using a rib to prevent it from bending. On one end of the stick, a part with 4 screw holes is attached using a tiny piece (1 mm thick) that locks them together. The camera is connected to this part using M2 bolts and hexagonal nuts.

The other end of the stick has two slots, which fit M4 bolts and nuts to connect to the bottom part of an enclosure that holds the projector. This enclosure consists of 6 parts that can be connected by sliding them together. The bottom part of the enclosure has a single hole in the front and a curved slot in the back. As a result, the enclosure can be shifted along the slots in the stick and rotated around the hole in the front. Furthermore, the holes in the enclosure make sure the SD-card, power supply and focus can still be accessed.

This structure is connected to a supporting structure. The supporting structure is made to fit the pipe, such that the ASV structure is approximately in the center of the pipe and oriented approximately parallel to the pipe.

Figure 17 shows a picture of the designed ASV setup.

4.3 Pipe setups

Measurements are performed using several pipe setups, which are summarized in figure 18. In the first, there is a long straight pipe with a light blocking obstacle at the end, to prevent light from entering the pipe. In the second setup, there is a 90 degree turn attached to the long straight pipe, with the light blocking obstacle placed after the turn. The third and fourth setup have a T-junction in two different configurations, in both cases using 2 light blocking elements. The last pipe is a large curve.

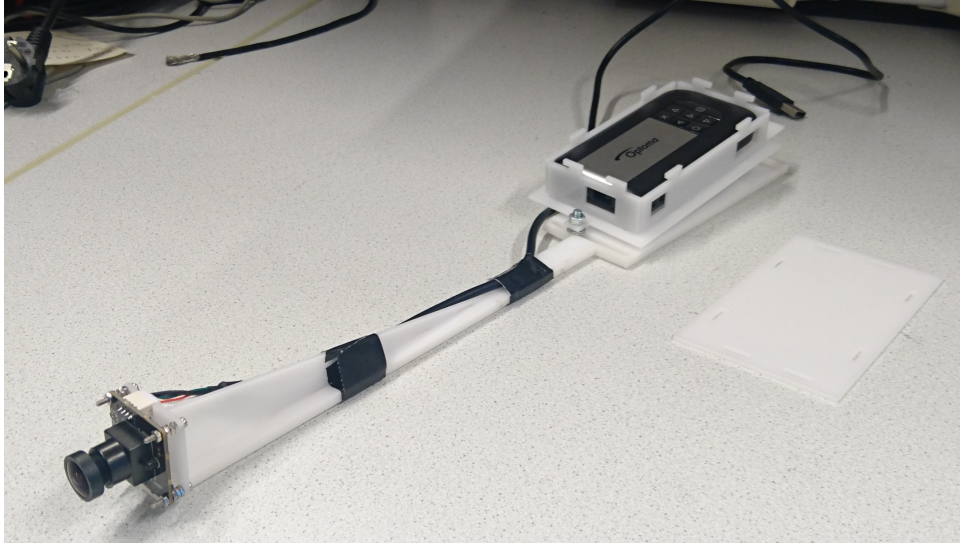


Figure 17: Camera and projector inside the ASV structure

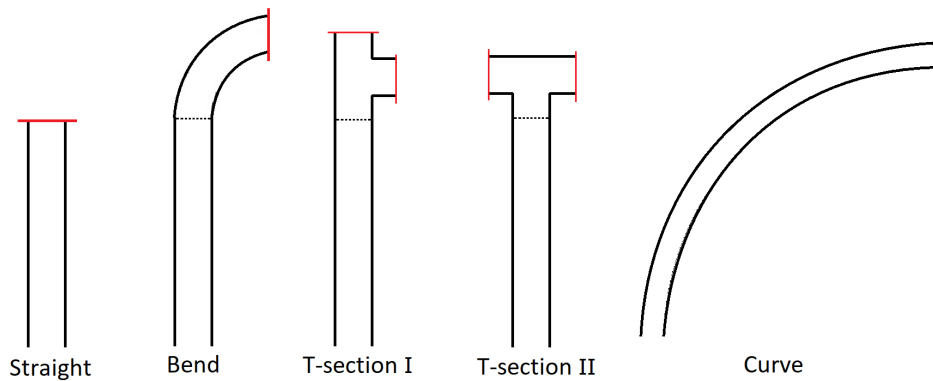


Figure 18: Pipe setups used in the experiments

4.4 Experiment design

The steps used in the measurement procedure can be listed as follows:

1. Calibrate the camera using the calibration procedure described in section 3.2.1.
2. Generate the patterns that are to be projected, preferably in a lossless file format using the same resolution that is native to the projector.
3. Transport the files to the projector using an SD-card. The other option in this step would be to connect the projector to a computer using a VGA cable. This is not recommended since a VGA cable is often

relatively inflexible, causing the ASV setup to clamp itself to the inner pipe wall and around tight turns.

4. Calibrate the extrinsic ASV parameters by following the procedure described in section 3.2.2.
5. Calibrate the projector using the procedure described in section 3.2.3.
6. Connect the ASV setup to the supporting structure and place it into the pipe setup.
7. Take an image with the camera and save the grayscale layer.
8. Push the ASV setup a little further into the pipe.
9. Repeat step 7 and 8 until the setup cannot be pushed any further
10. Repeat step 6-9 for all patterns being tested, as discussed in section 3.3
11. Repeat step 6-10 for all different pipe setups, as discussed in section 4.3

5 Results

5.1 Straight, Bend and T-section I

From the measurement images and their respective 2D and 3D reconstructions, a selection has been made that best serves to illustrate the arguments made in the conclusion and discussion. For the measurements performed in the Straight, Bend of T-section I pipe setups, these results can be found in section 7.4. Furthermore, a measurement image for each of the pipe setups is repeated in figure 19.

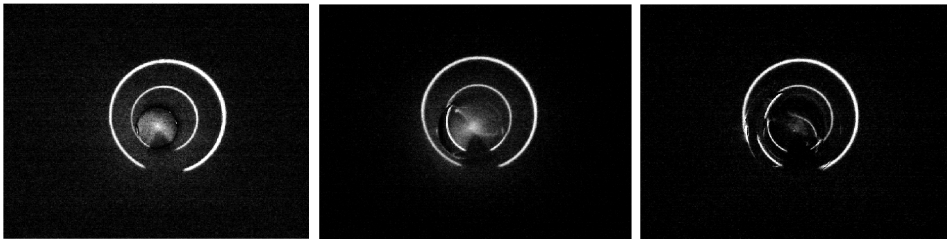


Figure 19: Measurement images for different pipe setups, 'Concentric', $N=2$. Left: Straight, Middle: Bend, Right: T-section I

5.2 Curve

The limited measurement range of the ASV setup is most apparent in the measurement images taken in the curved pipe, as described in section 4.3. In the images, examples in figure 20, it can be seen that not the entire or any detectable part is wholly in the image. Therefore, no further image processing steps have been applied.

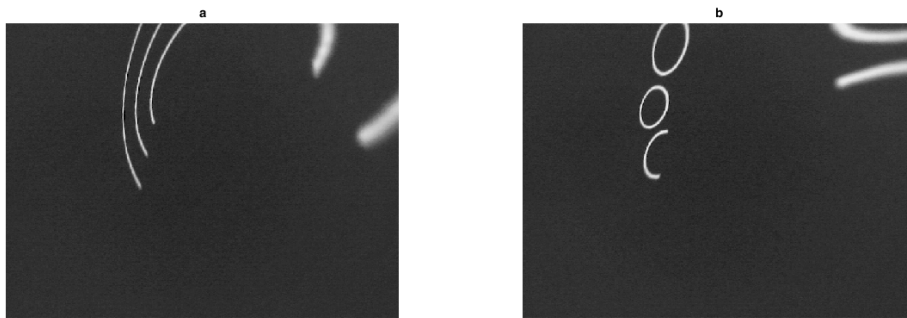


Figure 20: Measurement images in the curved pipe. Left: Concentric, $N=3$, Right: Radial, $M = 12$

5.3 T-section II

In the second variation of the T-section pipe setup, also described in section 4.3, there was a different problem with the measurement images. Because the projector was aimed approximately straight at the back wall of the intersection, a lot of light reflected back towards the camera. The measurement images, examples in figures 21 show how the reflection can be seen in the form of a bright spot that connects the, otherwise separate, parts of the projected pattern. As a result, the image processing steps have also not been applied to measurement images from this pipe setup.

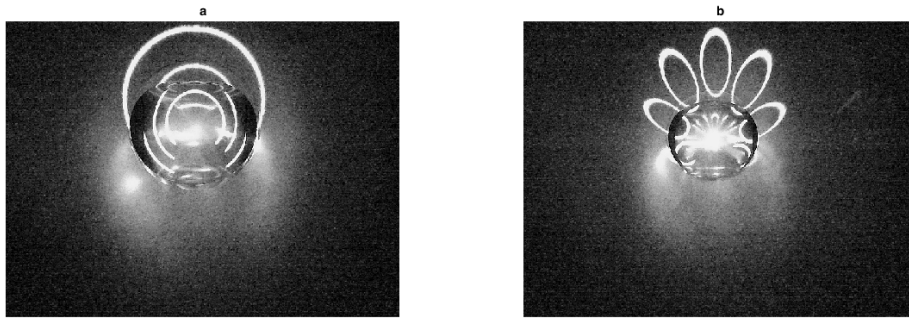


Figure 21: Measurement images in the T-section II pipe setup. Left: Concentric, $N=3$, Right: Radial, $M=8$

5.4 Errors

The errors that arose from the calibration procedure can be found in table 3. Furthermore, table 4 displays the average values of the errors in the radial and axial direction for each reconstructed part. Values are given for the concentric type pattern using $N=2$.

Table 3: Error values

Parameter	Δr_c	$\Delta \tan(\Phi)$	Δf_c	Δt_z
Value	1	0.1	2.53	5
Unit	pix	pix	mm/pix	mm

Table 4: Average errors in the radial and axial direction for different pipe setups using the concentric pattern (N=2)

Pipe	Average ΔR_c (mm)					Average ΔZ_c (%)				
Straight	0.80	0.80				1.59	1.99			
Bend	0.80	0.780	0.67			1.59	2.00	1.87		
T-section I	0.80	0.80	0.67	0.63	0.63	1.596	2.01	1.69	1.90	1.84

6 Final considerations

6.1 Discussion

Replicating laser light

There are some aspects that differ between the measurement setup and the scenario in which the PIRATE robot is performing measurement in a gas pipe underground.

First of all, the limited length of the pipes required the use of light blocking elements at the ends. As a result, the light is reflected back and creates a bright, fuzzy spot in the center of the image. The brighter the spot, the higher the threshold in image processing step 3, section 3.4.3, had to be, to be able to distinguish parts of the pattern as different objects in image processing step 4, section 3.4.4. This is best illustrated in figure 27. In this measurement image there are parts of 3 concentric circles close to each other, that are recognized and reconstructed as 1 object.

Using a higher threshold also tends to make the parts of the patterns that hit the pipe far away from the ASV setup undetectable, as these are not as bright as the parts that hit the pipe nearby. This is most clearly seen in figure 36. In this image a higher threshold had to be used such that the center spot was not part of the selected object. As a result, the intersection of the pattern farthest from the camera was not detected and thus only a single curve was reconstructed.

Second, the projected shapes have thicker lines than would be possible using laser light. These thicker lines have the unfavorable effects of causing the measurement images to be brighter in general and having parts of the projected pattern overlap sooner, compared to thinner lines. If the patterns would have been generated with thinner lines, the effects of quantization would have been more apparent, which would increase the error in r_p .

Third, there is a 'gap' in every image, which is the result of the design of the ASV structure that keeps the camera and projector in place. Without the gap, constraints could have been imposed on the line that is fitted to the data in image processing step 8, section 3.4.8. For example in the 'concentric' case, the constraint would make sure the slope and position of the fitted curve are equal at the maximum and minimum angle of the polar

transform.

Concentric

In the straight pipe, the 'concentric' type pattern leads to an accurate reconstruction of the pipe's inner surface, as can be seen in figures 24, 25, 26 and 27. When multiple concentric circles are projected, $N > 1$, and the pipe is known to be straight, the reconstruction can be used to determine the ASV systems orientation and location with respect to the pipe. The bright spot in the center of the image gets brighter with higher values of N , but it does not interfere with object selection. Higher values of N yield more accurate determinations of the ASV systems position and orientation.

In case of the 'bend' pipe setup, measurement images where one or multiple concentric circles hit the bend can be found in figures 32, 33, 34 and 35. In the 2D reconstruction of these images there is a clear distinction in terms of radius along a part of inner concentric circles. The change in radius from the other reconstructed parts contains information on the angle of the turn, while the angular location gives information on the direction the bend goes. When multiple concentric circles are used, all parts of the pattern that hit the curve can be recognized as a single object, as in figure 35, leading to an inaccurate reconstruction. There is an optimal distance between concentric circles, from which an optimal value for N can be determined, depending on how much area of the pattern is blocked by the camera in the ASV system. As can be seen in figures 42, 43, 44 and 45, the concentric pattern is less suitable for detecting T-sections in this configuration. The reconstruction shows broken up parts of the pattern, indicating that there is sort of obstacle or intersection, but fails to display any useful information on the distance or size. Similar to the 'bend' pipe setup, angular location of the disruption does provide approximate information on the location of the intersection. The distance between concentric circles determines whether none, some, or all circles are influenced by the T-section, which imposes constraints on the minimum and maximum size in axial direction of the detected disturbance.

Radial: 'Intersections' & 'Min/Max'

In the straight pipe, the 'Intersections' and 'Min/Max' image processing methods show results comparable to having two concentric circles. However, when the intersections or minimum values are projected far away from the camera, they can become undetectable such as in figure 28. Because these image processing methods use less data points to make a reconstruction than the 'concentric' pattern, it is not as accurate for determining the position and orientation of the ASV system with respect to the pipe. Therefore, for higher values of M , there is more data available and the reconstruction tends to be more accurate.

In the bend pipe and the T-section, the 'Intersections' image processing method fail to detect anything but a straight pipe. This is either because not all intersections are detectable or there are too many false positive when detecting intersections. This is best illustrated by figure 46. Increasing M will increase the number of intersections, which increases accuracy, assuming all data points are extracted without false positives.

The 'Min/Max' image processing method reconstructs 2 curves in the bend pipe and T-junction, as seen in figures 38 and 47. While the farthest curve has a different slope, indicating that the pipe is not straight, it is impossible to distinguish whether there is a bend or T-section. Increasing M tends to increase accuracy.

Radial: 'Half circles'

In the straight pipe, the 'half circles' image processing method yields inaccurate results. Figure 31 exemplifies how in the 2D plot how the reconstructed curves all contain different radii, while the measurement image shows that the entire pattern hits the pipe wall. Different values for M yield similar results.

In case of the bend pipe, the 'half circles' method is capable of detecting the direction of the bend and approximately determine the angle. Figure 40 shows in its 2D view a smaller radius for 2 sections, indicating a bend in that direction. The slope of those curves in the 3D reconstruction can be used to determine the angle of the bend. In this pipe setup, the higher M, the more accurate the direction and angle of the bend can be determined.

In case of a T-section, the method is unable to detect the intersection. This is due gaps in the projected pattern, best exemplified in the measurement image in figure 48 . As a result, the detected objects are smaller than expected, leading to inaccurate reconstructions.

Errors

The calculated errors were similar for each pattern and pipe setup. As expected and described in section 3.1, the error in radial direction increases as the radius increases and the error in axial direction increases for reconstruction farther into the pipe. Furthermore, all errors were smaller than 1 mm.

Figure 31 exemplifies how the reconstructed points do not lie on a cylinder. Even with the calculated error boxes, a good fit can not be found. This leads to the conclusion that the error in determining the point correspondence between measurement images and patterns has a larger error than the error caused by calibration and quantization.

6.2 Conclusion

From the measurements on 'concentric' type patterns, it is concluded that this pattern is suitable for finding the position and orientation of the ASV system with respect to the pipe, if the pipe is known to be straight. Because this pattern has gaps in the axial direction, it is less suitable for finding distances to certain objects and more suitable for finding irregularities on the pipe's inner wall, along the radial direction.

Measurements on 'radial' type pattern, using the 'Intersections' and 'Min/Max' image processing steps yield results similar and less accurate compared to the 'concentric' type for $N = 2$. This was because not only less data points are available for reconstruction, some data points are undetectable in the measurement image and false positives occur often.

Furthermore, the 'Half circle' image processing method is concluded to be less accurate in straight pipes, compared to the 'concentric' type pattern. It does allow for detecting of obstacles along the axial direction, making it more suitable for distance estimation.

A pattern consisting of both concentric and radially aligned circles could bring out the best of both individual type of patterns. This pattern would consist of 2 or more concentric circles, that encapsulate a series of radially aligned circles. Given an intersection, bend, obstacle or other pipe setup, ideally at least 2 concentric circles will hit the pipe, while the radially aligned circles hit the intersection, bend or obstacle. The concentric circles would allow for the general pipe structure and position and orientation of the AVS setup to be determined, while the radially aligned circles provide details on the feature of interest. Examples of this pattern are given in figure 22.

The largest concentric circle is the full size of the image, while the smallest concentric circle has a radius such that it is just fully visible and not blocked by the camera that is in front of the projector or laser. The radially aligned circles would have an as large as possible radius while not touching or intersecting the concentric circles. Lastly, M would be chosen as large as possible, while making sure the radially aligned circles also do not intersect or touch.

6.3 Recommendations

Since the camera has a larger field of view than the projector, dark spots show up on measurement images on the location of intersections and bends. This is most clearly seen in figures 38 and 47, where patterns are broken up on the left side. Instead of reconstruction of the pipe based on where the pattern hits the wall, an analyses of these dark spots could be done to determine the location and direction of bends, intersections and possibly obstacles.

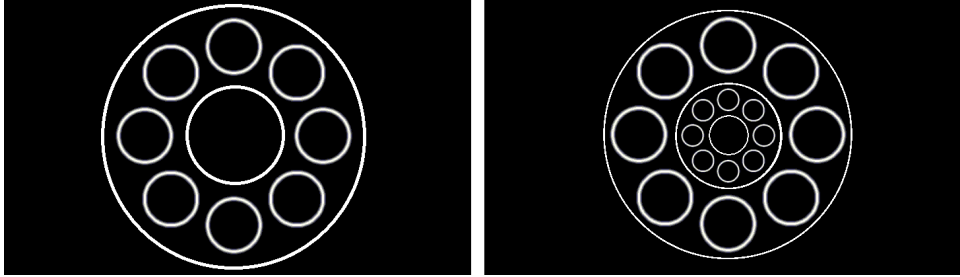


Figure 22: Examples of proposed patterns. Left: $N=2$, $M=8$, Right: $N=3$, $M=8$

Two patterns, shown in figure 23, are proposed that might be suitable for this. The pattern on the left is a variation of that shown on the left in figure 22, that uses lines instead of radially aligned circles. For this image the 2 image processing steps are required. First, if it detects which of the lines have been broken up, the direction the intersection or bend leads can be determined. Second, the distance between two halves of a broken up line reflects the size of the opening of the intersection or the angle of the bend. It is expected that the donut-like pattern show on the right in figure 23 will result in measurement images with very bright and very dark regions. The shape, size and location of the dark spots will contain information on the location, distance and size of the intersection or bend.



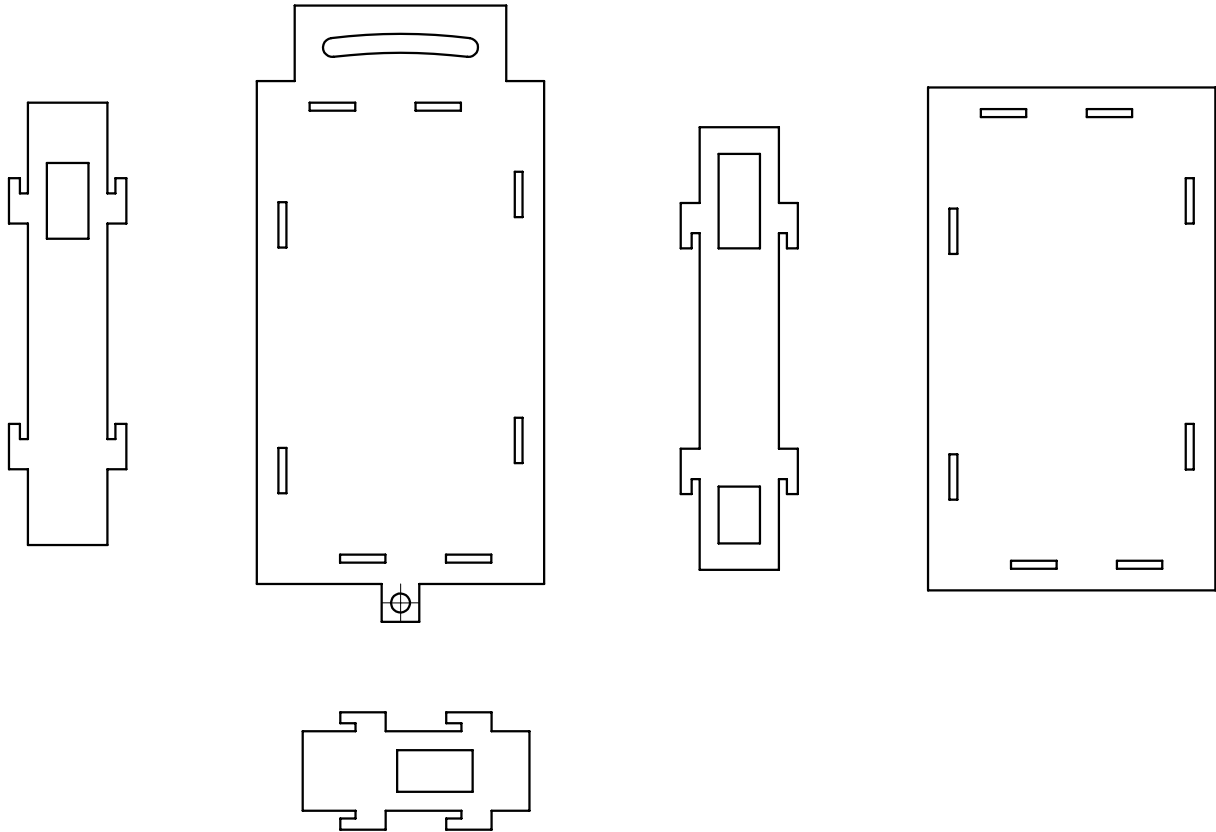
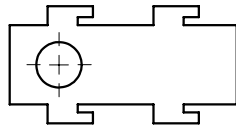
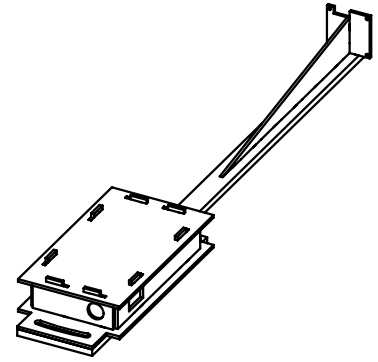
Figure 23: Suggestions for patterns to be tested, with $N=2$. Left: Lines instead of radially aligned circles. Right: Donut-like instead of radially aligned circles

7 Appendix

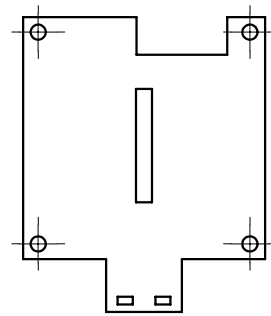
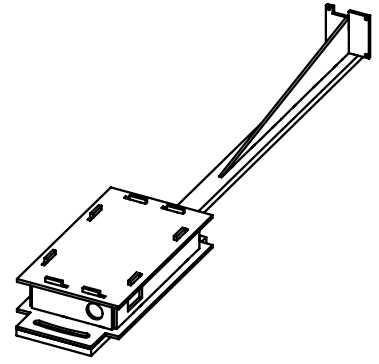
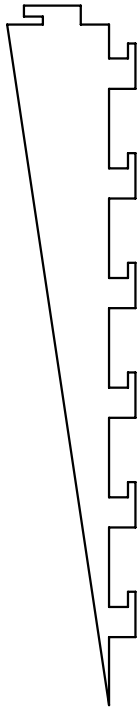
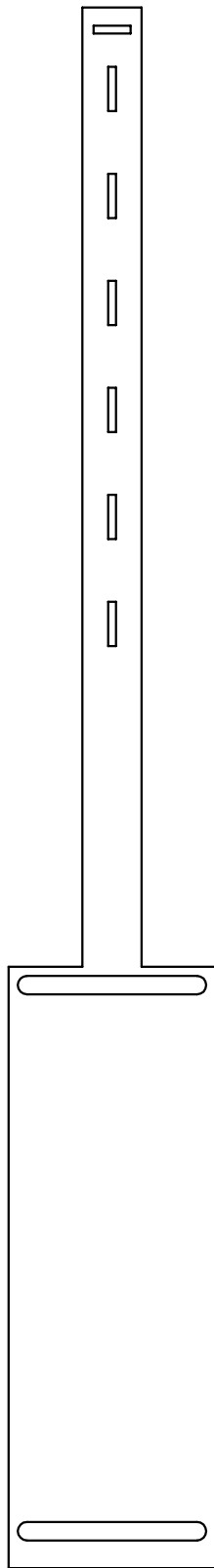
7.1 Table of symbols & units

Symbol	Parameter	Unit
Ψ	Coordinate system in \mathbb{R}^3	mm
ψ	Image plane coordinate system in \mathbb{R}^2	pix
$\mathbf{R} = [x_r, y_r]$	Principal point	pix
F	Focal length	mm
$\mathbf{P} = [P_x, P_x, P_z]$	Any point P	mm
$\mathbf{Q} = [x_q, y_q]$	Corresponding point in image	pix
s	Skew factor	-
Φ	Angle between camera plane axis	-
f_x, f_y, f_i	Normalized focal lengths	mm/pix
n_x, n_y	Size of single pixel	mm
N_x, N_y	Total size of image sensor	mm
\mathbf{K}	Camera/projector matrix	-
$\tilde{\mathbf{Q}} = [\tilde{x}_q, \tilde{y}_q]$	Undistorted pixel coordinates	pix
$\mathbf{D} = [x_d, y_d]$	Distortion center	pix
L(r)	Distortion factor	-
k_n	Radial distortion coefficients	-
r	Distance from distortion center	pix
ν	Field of view (FOV)	rad
\mathbf{t}_c^P	Translation matrix	-
\mathbf{R}_c^P	Rotation matrix	-
α, β, ζ	Angle about x-, y-, and z-axis	rad
t_x, t_y, t_z	Translation along x-, y-, and z-axis	mm
\mathbf{e}	Epipole	-
\mathbf{F}	Fundamental matrix	-
ϕ	Cone half-fan angle	rad
Δ ""	Error in ""	-
N	Number of concentric cones	-
M	Number of radially aligned cones	-

7.2 ASV structure design



PROJECTION METHOD		UNLESS STATED OTHERWISE: TOLERANCES $\pm 0,5$ MM	DRAWN	--	DATE	16-Jul-18
			CHECKED	--	SCALE	1:2
MATERIAL	--	SURFACE TREATMENT	TITLE			REV.
	--		NO NAME			
UNIVERSITY OF TWENTE.			DRAWING NO.			A4
			--			
FACULTY OF ENGINEERING			FILE / PART NAME	Drawing		SHEET 1 OF 1
			DIMENSIONS IN MILLIMETERS			



PROJECTION METHOD		UNLESS STATED OTHERWISE: TOLERANCES $\pm 0,5$ MM	DRAWN	--	DATE	16-Jul-18
			CHECKED	--	SCALE	1:2
MATERIAL	--	SURFACE TREATMENT	TITLE			REV.
	--		NO NAME			01
UNIVERSITY OF TWENTE.			DRAWING NO.			A4
			--			
FACULTY OF ENGINEERING			FILE / PART NAME		SHEET 1 OF 1	
			Drawing 2			
			DIMENSIONS IN MILLIMETERS			

7.3 Code

The following code represents the most relevant pieces of the image processing steps. In the code, 'xxx' represents the location for any variation of 'FUNCTION1'. This is either a function that finds concentric circles, intersections, minimum and maximum values or halves of circles. 'FUNCTION2' and 'FUNCTION3' calculate the 3D reconstruction and corresponding errors respectively.

```
I = imread(measurement0.tif'); %input image
I2 = undistortImage(I,cameraParams); %undistorted image
I3 = medfilt2(I2); %median filter
I4 = I3;
indices = find(I4<(T*max(max(I4)))); %threshold
I4(indices) = 0;

for n = 1:N
I5(:,:,n) = selectobject(I4,T,n,connectivity); %select nth largest object
I6(:,:,n) = imdilate(I5(:,:,n),strel('square', 3)); %dilation
I7(:,:,n) = imadjust(I6(:,:,n)); %increase contrast

xxx

[curve, data] = fit(theta,rho,'fourier2','Weight',w); %calculate fit
coefficients = coeffvalues(curve);
a0 = coefficients(1);
a1 = coefficients(2);
b1 = coefficients(3);
a2 = coefficients(4);
b2 = coefficients(5);
freq = coefficients(6);

omega = linspace(min(theta),max(theta),points);
rc = a0 + a1*cos(omega*freq) + b1*sin(omega*freq) + a2*cos(2*omega*freq) + b2*sin(2*

[Zp,Rp] = FUNCTION2(rp,rc,tz,fxc,fyc,fxp,fyp,omega); %3D reconstruction
[DRp,DZp] = FUNCTION3(Zp,Rp,rc,rp,tz,fxc,fyc,omega,Drc,Drp,Dtz,Dfx,Dfy); %correspond
end

FUNCTION1: Concentric

[y,x] = find(I); %list position of nonzero elements
for i = 1:length(x)
    w(i) = I(y(i),x(i)); %make list of weights for every position
end
```

```

x = x - rx; %shift such that image center is at 0,0
y = y - ry;
[theta,rho] = cart2pol(x,y); %convert to polar coordinates

```

FUNCTION1: Intersections

```

skel= bwmorph(I7,'skel',Inf); %skeletonize, remove endpoints
B = bwmorph(skel, 'branchpoints');
E = bwmorph(skel, 'endpoints');
[y,x] = find(E);
B_loc = find(B);
Dmask = false(size(skel));
for k = 1:numel(x)
    D = bwdistgeodesic(skel,x(k),y(k));
    distanceToBranchPt = min(D(B_loc));
    Dmask(D < distanceToBranchPt) =true;
end
I8 = skel - Dmask;

I9 = bwmorph(I8, 'diag'); %fill in diagonal
I9 = bwmorph(I9, 'skel', inf); %re-skeletonize
I9 = bwmorph(I9, 'spur'); %remove spurs
I10 = bwmorph(I9, 'branchpoints'); %find branchpoints

[theta, rho] = {FUNCTION1:Concentric}(I10(:,:,n));

```

FUNCTION1: Min/Max

```

[theta, rho] = FUNCTION0(I7(:,:,n));

maxindex = find(rho==max(rho));
minindex = find(rho==min(rho));
Rmax(n,1) = rho(maxindex);
Rmin(n,1) = rho(minindex);
Tmax(n,1) = theta(maxindex);
Tmin(n,1) = theta(minindex);

rho = [Rmin,Rmax];
theta = [Tmin,Tmax];

```

FUNCTION1: Half circles

```

[y,x] = find(k); %list position of nonzero elements
for i = 1:length(x)
    w(i) = k(y(i),x(i)); %make list of weights for every position

```

```

end
x = x - rx; %shift such that image center is at 0,0
y = y - ry;

xmid = (max(x) + min(x)) / 2; %calculate centerpoint of blob
ymid = (max(y) + min(y)) / 2;
x(end+1) = xmid; %save centerpoint to display later
y(end+1) = ymid;
w(end+1) = 0;
[theta,rho] = cart2pol(x,y); %convert to polar coordinates
for i = 1:length(theta)
    if theta(i) < -1/2*pi
        theta(i) = theta(i) + 2*pi;
    end
end
index = find(rho==max(rho)); %discard radii smaller than centerpoint
for i = 1:length(rho)
    if rho(i) < rho(end)
        w(i) = 0;
    end
end
end

```

FUNCTION2

```

term1 = (-(tz*Xqp^2)/fxp^2) - ((tz*Yqp^2)/fyp^2);
term2_nomi = sqrt((fyc^2*fyp^2*tz^2*Xqc^2*Xqp^2) + (fxc^2*fyp^2*tz^2*Xqp^2*Yqc^2) +
term2_denom = (fxc*fxp*fyc*fyp);
denominator = ((Xqc^2/fxc^2) - (Xqp^2/fxp^2) + (Yqc^2/fyc^2) - (Yqp^2/fyp^2));

Zp(i) = ((term1 + (term2_nomi/term2_denom))/denominator);
Rp(i) = sqrt((Zp(i)^2*((fyc^2*Xqc^2) + (fxc^2*Yqc^2))) / (fxc^2 + fyc^2));

```

FUNCTION3

```

DZpDrc = abs(-Zp ./ (rc-rp )) * Drc;
DZpDrp = abs((rc * tz) / (rp -rc).^2) * Drp;
DZpDtz = abs(Zp ./ tz) * Dtz;
DZp = sqrt(DZpDrc.^2 + DZpDrp.^2 + DZpDtz.^2);

DRpDrc = abs(Zp / (fx+fy)/2) * Drc;
DRpDfc = abs(-Rp / (fx+fy)/2) * (Dfx+Dfy)/2;
DRpDtz = abs(Rp / tz) .* Dtz;
DRp = sqrt(DRpDrc.^2 + DRpDfc.^2 + DRpDtz.^2);

```

7.4 Results

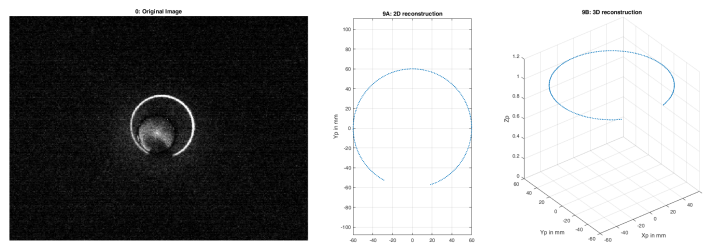


Figure 24: Straight, Concentric, $N=1$

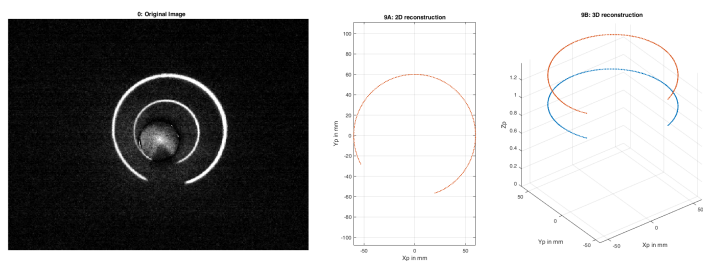


Figure 25: Straight, Concentric, $N=2$

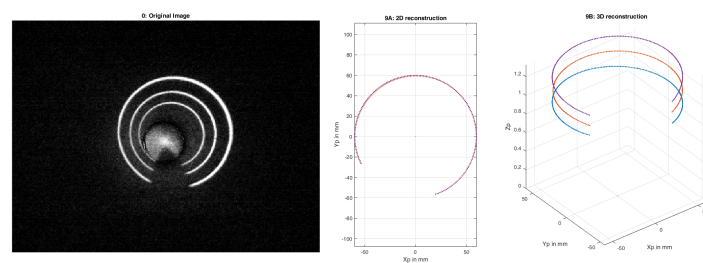


Figure 26: Straight, Concentric, $N=3$

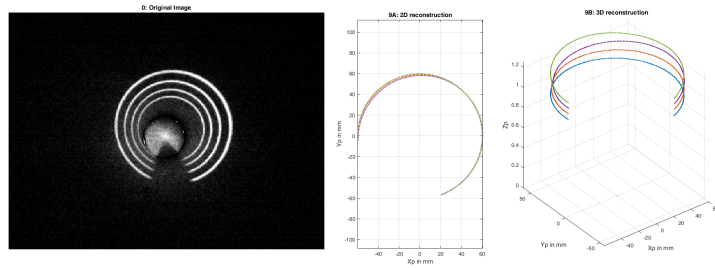


Figure 27: Straight, Concentric, $N=4$

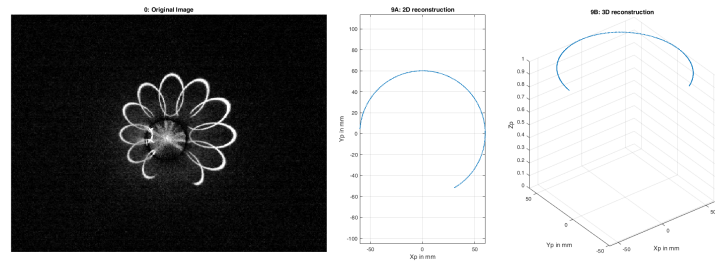


Figure 28: Straight, Radial: Intersections, $M=12$

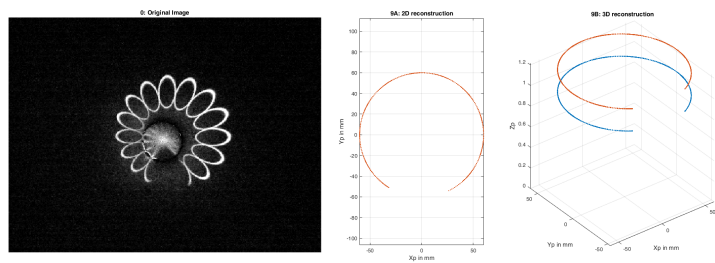


Figure 29: Straight, Radial: Intersections, $M=16$

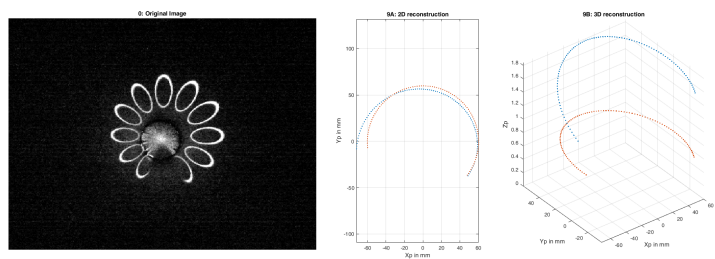


Figure 30: Straight, Radial: Min/Max, $M=12$

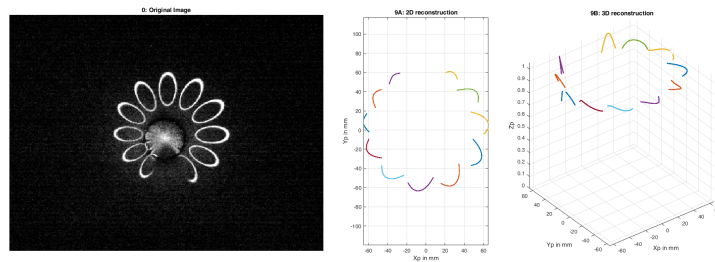


Figure 31: Straight, Radial: Half circles, $M=12$

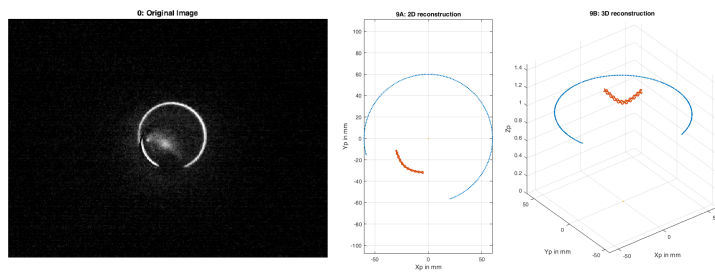


Figure 32: Bend, Concentric, $N=1$

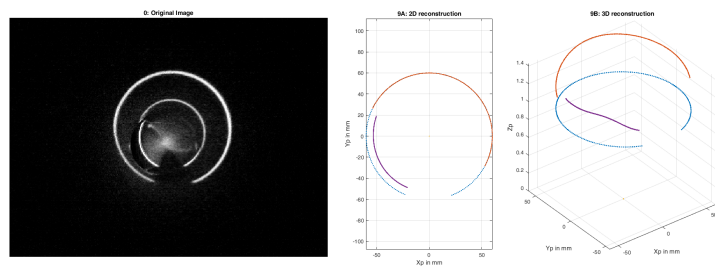


Figure 33: Bend, Concentric, $N=2$

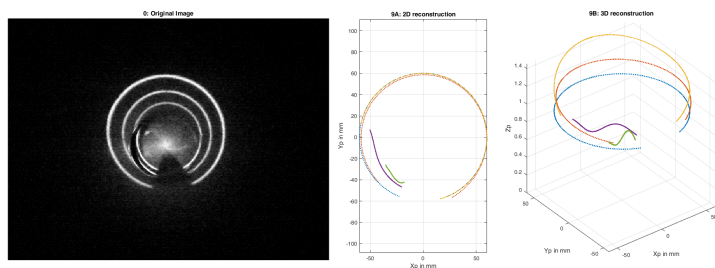


Figure 34: Bend, Concentric, $N=3$

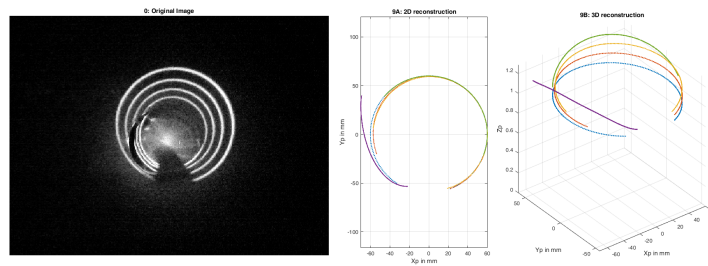


Figure 35: Bend, Concentric, $N=4$

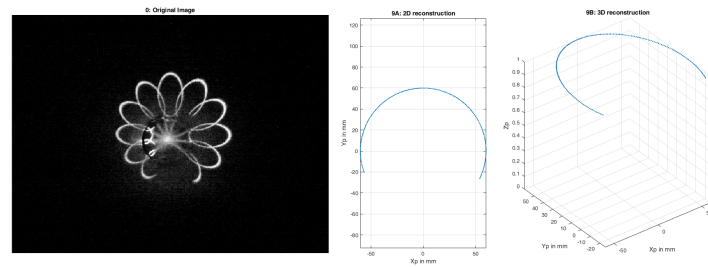


Figure 36: Bend, Radial: Intersections, $M=12$

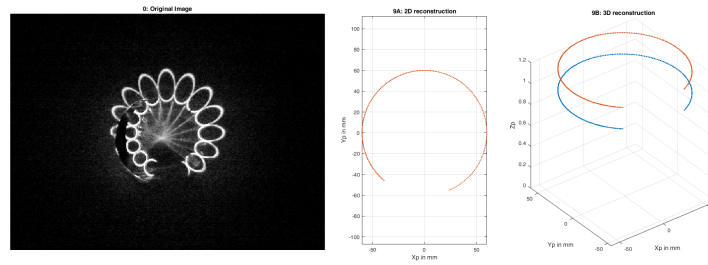


Figure 37: Bend, Radial: Intersections, $M=16$

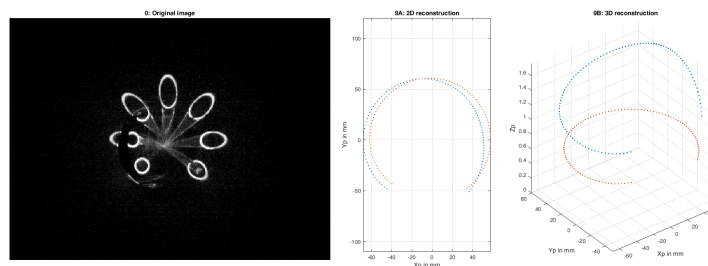


Figure 38: Bend, Radial: Min/Max, $M=8$

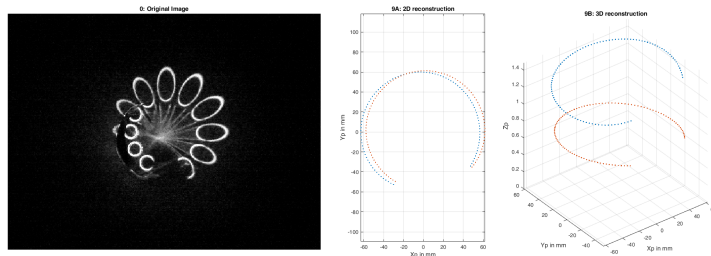


Figure 39: Bend, Radial: Min/Max, $M=12$

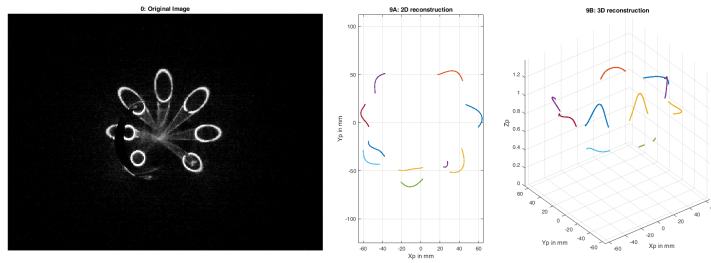


Figure 40: Bend, Radial: Half circles, $M=8$

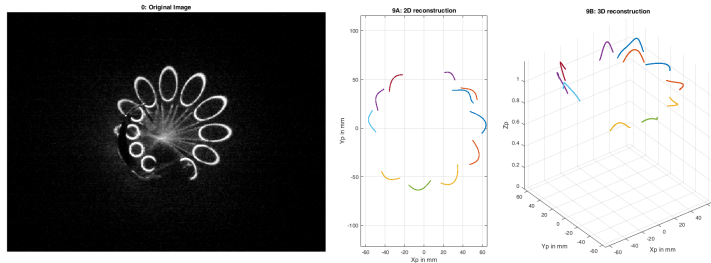


Figure 41: Bend, Radial: Half circles, $M=12$

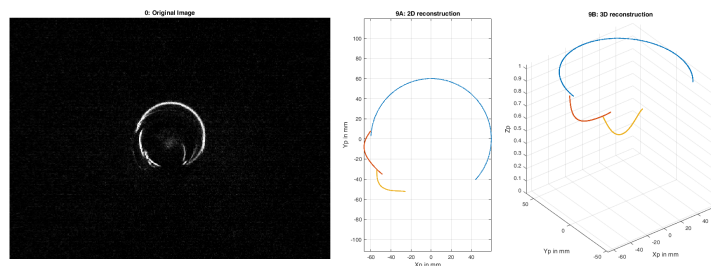


Figure 42: T-section I, Concentric, $N=1$

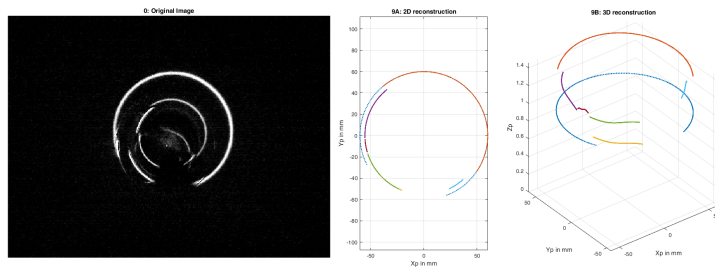


Figure 43: T-section I, Concentric, $N=2$

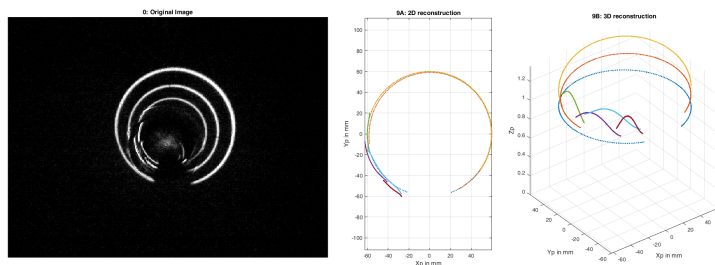


Figure 44: T-section I, Concentric, $N=3$

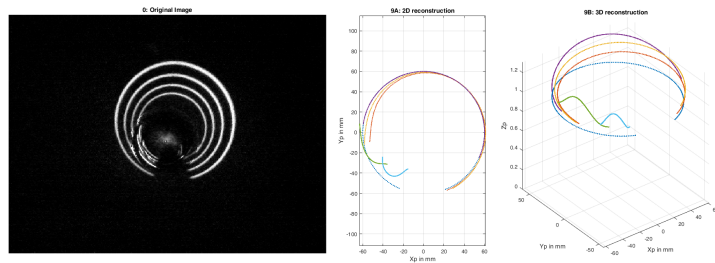


Figure 45: T-section I, Concentric, $N=4$

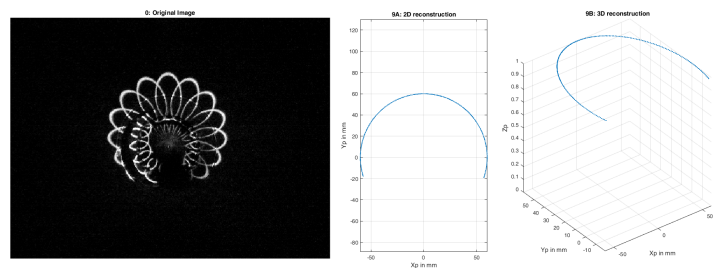


Figure 46: T-section I, Radial: Intersections, $M=16$

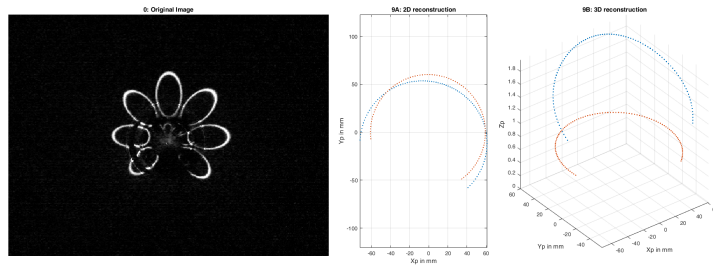


Figure 47: T-section I, Radial: Min/Max, $M=8$

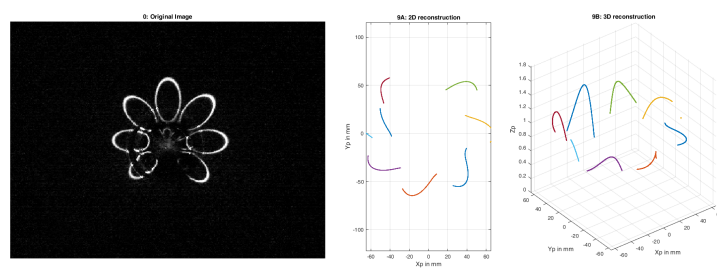


Figure 48: T-section I, Radial: Half circles, $M=8$

References

- [1] Robotics and Mechatronics, Smart Tooling, University of Twente, 27 March 2018, <https://www.ram.ewi.utwente.nl/research/project/smart-tooling.html>
- [2] Smart Tooling, Interreg Vlaanderen-Nederland, Europees Fonds voor Regionale Ontwikkelingen, <http://smarttooling.eu/>
- [3] Robotics and Mechatronics, PIRATE, University of Twente, 27 March 2018, <https://www.ram.ewi.utwente.nl/research/project/pirate.html>
- [4] Pipe Inspection Robot for AuTonomous Exploration, 27 March 2018, <http://inspectierobot.edwindertien.nl/>
- [5] Measurement system for pipe profiling, E. Drost, 2009, University of Twente
- [6] Implementation of a Monocular Structured Light Vision System for Pipe Inspection Robot PIRATE, M. Reiling, 2014, University of Twente
- [7] Design of an inspection robot for small diameter gas distribution mains, E.C. Dertien, 2014, DOI: 10.3990/1.9789036536813, ISBN: 9789036536813, University of Twente
- [8] CS231A Course Notes 1: Camera Models, Kenji Hata and Silvio Savarese, Stanford, Winter 2018, <https://web.stanford.edu/class/cs231a>
- [9] Camera Calibration Toolbox for Matlab, Jean-Yves Bouguet, *http* : [//www.vision.caltech.edu/bouguetj/calibdoc/](http://www.vision.caltech.edu/bouguetj/calibdoc/)
- [10] Multiple View Geometry in Computer Vision, Hartley, Richard and Zisserman, Andrew, 2003, Cambridge University Press, ISBN: 0521540518
- [11] A Simple and Efficient Method for Radial Distortion Estimation by Relative Orientation, Y. Duan and X. Ling and Y. Zhang and Z. Zhang and X. Liu and K. Hu, IEEE Transactions on Geoscience and Remote Sensing, 2017, DOI: 10.1109/TGRS.2017.2735188
- [12] A flexible new technique for camera calibration, Z. Zhang, IEEE Transactions on Pattern Analysis and Machine Intelligence, 2000, DOI: 10.1109/34.888718
- [13] Image adapted from: <https://en.wikipedia.org/wiki/File:Pinhole.svg>
- [14] Image adapted from: What Is Camera Calibration?, Matlab, <https://nl.mathworks.com/help/vision/ug/camera-calibration.html>
- [15] cart2pol, Matlab, <https://nl.mathworks.com/help/matlab/ref/cart2pol.html>